



ARL-TR-8725 • JUNE 2019



Imaging Study for Small Unmanned Aerial Vehicle (UAV)-Mounted Ground-Penetrating Radar: Part II – Numeric Examples and Performance Analysis

by Traian Dogaru

Approved for public release; distribution is unlimited.

NOTICES

Disclaimers

The findings in this report are not to be construed as an official Department of the Army position unless so designated by other authorized documents.

Citation of manufacturer's or trade names does not constitute an official endorsement or approval of the use thereof.

Destroy this report when it is no longer needed. Do not return it to the originator.



Imaging Study for Small Unmanned Aerial Vehicle (UAV)-Mounted Ground-Penetrating Radar: Part II – Numeric Examples and Performance Analysis

by Traian Dogaru

Sensors and Electron Devices Directorate, CCDC Army Research Laboratory

REPORT DOCUMENTATION PAGE

Form Approved
OMB No. 0704-0188

Public reporting burden for this collection of information is estimated to average 1 hour per response, including the time for reviewing instructions, searching existing data sources, gathering and maintaining the data needed, and completing and reviewing the collection information. Send comments regarding this burden estimate or any other aspect of this collection of information, including suggestions for reducing the burden, to Department of Defense, Washington Headquarters Services, Directorate for Information Operations and Reports (0704-0188), 1215 Jefferson Davis Highway, Suite 1204, Arlington, VA 22202-4302. Respondents should be aware that notwithstanding any other provision of law, no person shall be subject to any penalty for failing to comply with a collection of information if it does not display a currently valid OMB control number.

PLEASE DO NOT RETURN YOUR FORM TO THE ABOVE ADDRESS.

1. REPORT DATE (DD-MM-YYYY) June 2019		2. REPORT TYPE Technical Report		3. DATES COVERED (From - To) September 2018–January 2019	
4. TITLE AND SUBTITLE Imaging Study for Small Unmanned Aerial Vehicle (UAV)-Mounted Ground-Penetrating Radar: Part II – Numeric Examples and Performance Analysis				5a. CONTRACT NUMBER	
				5b. GRANT NUMBER	
				5c. PROGRAM ELEMENT NUMBER	
6. AUTHOR(S) Traian Dogaru				5d. PROJECT NUMBER	
				5e. TASK NUMBER	
				5f. WORK UNIT NUMBER	
7. PERFORMING ORGANIZATION NAME(S) AND ADDRESS(ES) CCDC Army Research Laboratory 2800 Powder Mill Rd ATTN: FCDD-RLS-RU Adelphi, MD 20783-1138				8. PERFORMING ORGANIZATION REPORT NUMBER ARL-TR-8725	
9. SPONSORING/MONITORING AGENCY NAME(S) AND ADDRESS(ES)				10. SPONSOR/MONITOR'S ACRONYM(S)	
				11. SPONSOR/MONITOR'S REPORT NUMBER(S)	
12. DISTRIBUTION/AVAILABILITY STATEMENT Approved for public release; distribution unlimited.					
13. SUPPLEMENTARY NOTES					
14. ABSTRACT This report investigates the possible configurations of a ground-penetrating radar (GPR) system installed on a small unmanned aerial vehicle platform and used for buried target imaging. The second part of this study presents a large set of numerical examples of synthetic aperture images obtained with such a radar system. The primary approach consists of simulating the point spread function of the system working in either down-looking or side-looking configuration, horizontal-horizontal or vertical-vertical polarization. Both 2-D and 3-D GPR imaging systems are considered in this work, emphasizing the advantages of certain sensing modalities over the others. Image attributes such as resolution, grating lobes, signal strength, ground bounce separation, and surface clutter sensitivity are used in the performance comparison. Additionally, we include images based on realistic radar models involving a buried antitank landmine and obtained via simulations with the AFDTD software.					
15. SUBJECT TERMS ground-penetrating radar, synthetic aperture radar, radar imaging, point spread function, radar modeling					
16. SECURITY CLASSIFICATION OF:			17. LIMITATION OF ABSTRACT UU	18. NUMBER OF PAGES 78	19a. NAME OF RESPONSIBLE PERSON Traian Dogaru
a. REPORT Unclassified	b. ABSTRACT Unclassified	c. THIS PAGE Unclassified			19b. TELEPHONE NUMBER (Include area code) (301) 394-1482

Contents

List of Figures	iv
List of Tables	viii
1. Introduction	1
2. Review of Configurations and Theoretical Formulation	2
3. PSF Analysis of a 2-D GPR SAR System	5
3.1 Numeric Examples of PSF for 2-D GPR	5
3.2 Image Resolution	14
3.3 Image Grating Lobes	20
3.4 Impact of Target Depth on GPR Images	23
3.5 Choice of Frequency and Bandwidth	26
3.6 Radar Signal Power	28
3.7 Effect of Positioning Errors	29
4. Modeling GPR SAR Imaging System for Buried Landmines	32
5. PSF Analysis of a 3-D GPR SAR System	39
5.1 Coherent GPR SAR System Using a 2-D Synthetic Aperture	40
5.2 Noncoherent GPR Imaging Using Multiple SAR Systems	54
6. Conclusions	62
7. References	65
List of Symbols, Abbreviations, and Acronyms	67
Distribution List	68

List of Figures

Fig. 1	Schematic representation of the GPR SAR system using a linear synthetic aperture in down-looking configuration: a) perspective view; b) top view; c) side view	3
Fig. 2	Schematic representation of the GPR SAR system using a linear synthetic aperture in side-looking configuration: a) perspective view; b) top view	3
Fig. 3	Graphic representation of the PSF for the GPR system operating in down-looking configuration and H-H polarization, with the point target placed at $x_0 = 0$, $y_0 = 0$, and $d = 0.1$ m: a) $z = -0.1$ m and x-z planes, perspective view; b) $z = 0$ and x-z planes, perspective view; c) x-z and y-z planes, perspective view; d) x-z plane. The SAR images in this figure include the ground bounce.....	7
Fig. 4	Graphic representation of the PSF for the GPR system operating in down-looking configuration and H-H polarization, with the point target placed at $x_0 = 0$, $y_0 = 0$, and $d = 0.1$ m: a) x-z and y-z planes, perspective view; b) x-z plane. The SAR images in this figure do not include the ground bounce.....	8
Fig. 5	Graphic representation of the PSF for the GPR system operating in down-looking configuration and V-V polarization, with the point target placed at $x_0 = 0$, $y_0 = 0$, and $d = 0.1$ m: a) $z = -0.1$ m and x-z planes, perspective view; b) $z = 0$ and x-z planes, perspective view; c) x-z and y-z planes, perspective view; d) x-z plane. The SAR images in this figure include the ground bounce.....	9
Fig. 6	Graphic representation of the PSF for the GPR system operating in down-looking configuration and V-V polarization, with the point target placed at $x_0 = 0$, $y_0 = 0$, and $d = 0.1$ m: a) x-z and y-z planes, perspective view; b) x-z plane. The SAR images in this figure do not include the ground bounce.....	9
Fig. 7	Graphic representation of the PSF for the GPR system operating in side-looking configuration and H-H polarization, with the point target placed at $x_0 = 0$, $y_0 = 0$, and $d = 0.1$ m: a) x-z and y-z planes, perspective view; b) x-z plane	10
Fig. 8	Graphic representation of the PSF for the GPR system operating in side-looking configuration and V-V polarization, with the point target placed at $x_0 = 0$, $y_0 = 0$, and $d = 0.1$ m: a) x-z and y-z planes, perspective view; b) x-z plane	11
Fig. 9	The aperture amplitude taper function characterizing the GPR system for various dipole antenna orientations in a) down-looking configuration; b) side-looking configuration with $Y_{\text{off}} = 1.5$ m. In both cases, the antennas are placed at $h = 1$ m and the frequency is 1.25 GHz.....	11

Fig. 10	Graphic representation in the x-z plane of the PSF for the GPR system operating in down-looking configuration and H-H polarization: a) image formed by the matched filter method described by Eq. 4; b) image formed by the inverse filter method described by Eq. 5	13
Fig. 11	Illustration of using a Hanning window for aperture tapering for the GPR system operating in side-looking configuration and V-V polarization: a) aperture amplitude taper function with and without the window at 1.25 GHz; b) PSF in the x-z plane	14
Fig. 12	Geometry of the GPR SAR system showing the parameters relevant to the resolution calculations: a) perspective view; b) side view along the y axis; c) side view along the x axis; d) image example in the x-z plane, showing the white dashed line along which the PSF is evaluated	16
Fig. 13	Main lobe of the PSF showing the cross-range resolution δx (half-width of the lobe) as a function of the lateral aperture offset Y_{off}	18
Fig. 14	Main lobe of the PSF showing the cross-range resolution δx (half-width of the lobe) as a function of the aperture integration length L, for: a) down-looking configuration; b) side-looking configuration with $Y_{off} = 3$ m. In both scenarios we used H-H polarization and $h = 1$ m.....	19
Fig. 15	Geometry of the GPR SAR system showing the parameters used in the calculations related to grating lobe spacing as a function of the aperture sampling rate.....	21
Fig. 16	PSF for the GPR system operating in down-looking configuration and H-H polarization, for the same parameters as in Fig. 4, emphasizing the cross-range grating lobes	22
Fig. 17	PSF for the GPR system operating in down-looking configuration and H-H polarization, with the point target buried at a) $d = 0.1$ m and b) $d = 0.2$ m	23
Fig. 18	PSF for the GPR system for the following configurations: a) $d = 0.1$ m, H-H, down-looking; b) $d = 0.2$ m, H-H, down-looking; c) $d = 0.1$ m, V-V, down-looking; d) $d = 0.2$ m, V-V, down-looking; e) $d = 0.1$ m, H-H, side-looking; f) $d = 0.2$ m, H-H, side-looking; g) $d = 0.1$ m, V-V, side-looking; and h) $d = 0.2$ m, V-V, side-looking. The ground bounce was not included in these images.	25
Fig. 19	PSF of the GPR system in down-looking configurations and H-H polarization, with the point target placed at a depth $d = 0.15$ m and operating in the following frequency bands: a) 0.5 to 2.5 GHz; b) 0.5 to 1.5 GHz; c) 1.5 to 2.5 GHz.....	27
Fig. 20	Graphic representation of the PTR amplitude factor as a function of the y direction aperture offset and various dipole antenna polarizations, at 1.25 GHz, for a) $x = 0$ and b) $x = 1$ m.....	29

Fig. 21	PSF of the GPR system in down-looking configurations and H-H polarization, with the point target placed at a depth $d = 0.2$ m, before and after introducing positioning errors: a) no errors; b) errors with 1.4-cm RMS; c) errors with 2.8-cm RMS; d) errors with 4.2-cm RMS. Note that all images are scaled to the same maximum voxel magnitude.....	31
Fig. 22	PSF of the GPR system in side-looking configurations and H-H polarization, with the point target placed at a depth $d = 0.2$ m, before and after introducing positioning errors: a) no errors; b) errors with 1.4-cm RMS; c) errors with 2.8-cm RMS; d) errors with 4.2-cm RMS. Note that all images are scaled to the same maximum voxel magnitude.....	31
Fig. 23	Representation of the AFDTD modeling geometry used by the GPR SAR system for imaging a buried M15 landmine, showing the top and side views with the relevant dimensions and parameters	33
Fig. 24	SAR image of the buried M15 landmine obtained with the GPR system in down-looking configuration and H-H polarization: a) x-z and y-z planes, perspective view; b) same as in a) with target overlay; c) x-z plane; d) same as in c) with target overlay	34
Fig. 25	SAR image of the buried M15 landmine obtained with the GPR system in down-looking configuration and H-H polarization, with the ground bounce removed: a) x-z plane image; b) x-z plane image with target overlay	34
Fig. 26	SAR image of the buried M15 landmine obtained with the GPR system in down-looking configuration and V-V polarization: a) x-z and y-z planes, perspective view; b) x-z plane	35
Fig. 27	SAR image of the buried M15 landmine obtained with the GPR system in side-looking configuration and H-H polarization: a) perspective view; b) y-z and x-z planes, respectively.....	36
Fig. 28	SAR image of the buried M15 landmine obtained with the GPR system in side-looking configuration and V-V polarization: a) perspective view; b) y-z and x-z planes, respectively.....	37
Fig. 29	SAR image of the M15 landmine buried under a rough ground surface obtained with the GPR system in down-looking configuration and H-H polarization: a) x-z and y-z planes, perspective view; b) x-z plane....	38
Fig. 30	SAR image of the M15 landmine buried under a rough ground surface obtained with the GPR system in down-looking configuration and V-V polarization: a) x-z and y-z planes, perspective view; b) x-z plane....	38
Fig. 31	SAR image of the M15 landmine buried under a rough ground surface obtained with the GPR system in side-looking configuration and H-H polarization: a) x-z and y-z planes, perspective view; b) x-z plane....	39
Fig. 32	SAR image of the M15 landmine buried under a rough ground surface obtained with the GPR system in side-looking configuration and V-V polarization: a) x-z and y-z planes, perspective view; b) x-z plane....	39

Fig. 33	Schematic representation of the GPR SAR system using a 2-D aperture for the formation of 3-D images: a) down-looking configuration, perspective view; b) down-looking configuration, top view; c) side-looking configuration, top view. The pink dots represent the aperture sample positions.....	41
Fig. 34	Aperture amplitude weighting functions for the 2-D synthetic aperture considered in this section for: a) down-looking configuration, H-H polarization; b) down-looking configuration, V-V polarization; c) side-looking configuration, H-H polarization; d) side-looking configuration, V-V polarization. The 2-D maps are plotted in linear amplitude scale at a frequency of 1.25 GHz.....	42
Fig. 35	Simulated PSF of a GPR system using a down-looking 2-D aperture and H-H polarization: a) x-z and y-z planes, perspective view; b) x-z plane; c) y-z plane.....	43
Fig. 36	Simulated PSF of a GPR system using a down-looking 2-D aperture and V-V polarization: a) x-z and y-z planes, perspective view; b) x-z plane; c) y-z plane.....	44
Fig. 37	Simulated PSF of a GPR system using a down-looking symmetric 2-D aperture and V-V polarization: a) schematic representation of the aperture samples; b) aperture amplitude weighting function at 1.25 GHz; c) x-z and y-z planes, perspective view; d) y-z plane.....	45
Fig. 38	Simulated PSF of a GPR system using a side-looking 2-D aperture and H-H polarization: a) x-z and y-z planes, perspective view; b) x-z plane; c) y-z plane.....	46
Fig. 39	Simulated PSF of a GPR system using a side-looking 2-D aperture and V-V polarization: a) x-z and y-z planes, perspective view; b) x-z plane; c) y-z plane.....	47
Fig. 40	Geometry of the side-looking GPR SAR system for 3-D imaging showing the parameters relevant to the y-direction resolution calculations.....	48
Fig. 41	Schematic representation of the GPR SAR system using a zigzag-type of aperture for the formation of 3-D images: a) perspective view; b) top view. The pink dots represent the aperture sample positions.....	49
Fig. 42	Simulated PSF of a GPR system using a zig-zag aperture as described in Fig. 36 and H-H polarization: a) x-z and y-z planes, perspective view; b) x-z plane; c) y-z plane.....	50
Fig. 43	Simulated PSF of a GPR system using a zig-zag aperture as described in Fig. 36 and V-V polarization: a) x-z and y-z planes, perspective view; b) x-z plane; c) y-z plane.....	51
Fig. 44	Schematic representation of the GPR SAR system using a circular aperture for the formation of 3-D images: a) perspective view; b) top view. The pink dots represent the aperture sample positions.....	52

Fig. 45	Simulated PSF of a GPR system using a circular aperture as described in Fig. 44 and H-H polarization: a) x-z and y-z planes, perspective view; b) x-z and x-y planes, perspective view; c) x-z plane; d) y-z plane.....	53
Fig. 46	Simulated PSF of a GPR system using a circular aperture as described in Fig. 44 and V-V polarization: a) x-z and y-z planes, perspective view; b) x-z and x-y planes, perspective view; c) x-z plane; d) y-z plane.....	54
Fig. 47	Schematic representation of the GPR SAR system using two linear apertures for the noncoherent formation of 3-D images: a) perspective view; b) top view	55
Fig. 48	Illustration of the principle underlying the noncoherent SAR image combination, which allows one to resolve the target in the y direction	56
Fig. 49	Simulated PSF obtained through the noncoherent combination of the images created by two linear-aperture SAR systems described in Fig. 47, in H-H polarization: a) x-z and y-z planes, perspective view; b) x-z plane; c) y-z plane.....	57
Fig. 50	Simulated PSF obtained through the noncoherent combination of the images created by the linear-aperture SAR systems described in Fig. 47: a) x-z and y-z planes, perspective view; b) x-z plane; c) y-z plane	58
Fig. 51	Schematic representation of the GPR SAR system using two orthogonal linear apertures for the noncoherent formation of 3-D images: a) perspective view; b) top view.....	59
Fig. 52	Simulated PSF obtained through the noncoherent combination of the images created by two SAR systems with orthogonal apertures described in Fig. 51, in H-H polarization: a) x-z and y-z planes, perspective view; b) x-z plane; c) y-z plane	60
Fig. 53	Simulated PSF obtained through the noncoherent combination of the images created by two SAR systems with orthogonal apertures described in Fig. 51, in V-V polarization: a) x-z and y-z planes, perspective view; b) x-z plane; c) y-z plane	61

List of Tables

Table 1	Comparison of various GPR imaging system performance attributes between down-looking and side-looking configurations, H-H and V-V polarizations.....	14
Table 2	Peak voxel magnitudes for the PSF images in Figs. 21 and 22, before and after introducing positioning errors.....	32

1. Introduction

Detection of objects buried underground is a major application of radar technology dating back several decades. Ground-penetrating radar (GPR) has been employed for purposes as diverse as mapping soil layers, bedrocks, and water tables; finding buried utility lines; exploring archeological and forensic investigation sites; or assessing the structural integrity of roads, bridges, and runways. An important military application of GPR is the detection of buried explosive hazards—these include landmines, unexploded ordnance, and a wide variety of improvised explosive devices.

This report represents the second part of an investigation into the possibility of operating a GPR system mounted on a small unmanned aerial vehicle (sUAV). As discussed in the first part of this study,¹ sUAV-mounted sensors can perform the rapid surveillance of large areas, with minimal human supervision, while avoiding contact with the ground. Additionally, these devices can fly close to the ground, which involves smaller ranges, and therefore lower power, than conventional, high-altitude airborne radar platforms. In effect, the excellent size, weight, power, and cost characteristics of these sensors make them perfect candidates for the future of GPR technology.

The first part of this investigation presented a review of the main attributes required from a GPR system and the current state-of-the-art in this technology and described the proposed sUAV-based GPR configurations. Subsequently, we developed the modeling methodology, including the derivation of the point target response (PTR) and the imaging algorithm. The major items discussed in Part I are briefly summarized in Section 2 of the current report (Part II).

The remainder of this report presents a large number of numerical models analyzing the GPR imaging performance as a function of radar parameters that include frequency, polarization, and sensing geometry. Section 3 presents simulation results for the point spread function (PSF) obtained by a 2-D imaging geometry for various radar parameters. In Section 4 we include modeling results of a realistic target and deployment scenario, obtained by a full-wave electromagnetic (EM) scattering analysis software. Section 5 explores the possibility of creating 3-D synthetic aperture radar (SAR) images of buried targets using different aperture geometries. We finalize with conclusions in Section 6.

2. Review of Configurations and Theoretical Formulation

In this study we investigate the imaging performance that can be achieved by an sUAV-based GPR system working with ultra-wideband (UWB) waveforms and employing SAR processing techniques. The basic SAR system configuration consists of a pair of transmitter (Tx) and receiver (Rx) antennas that are physically moved along a linear track parallel to the ground surface, effectively scanning a given area for possible targets. One way to quantify the SAR system performance is to study the PSF, which is the image obtained by radar sensing of a point target. The PSF can be interpreted as the system's impulse response and its analysis is essential in establishing performance metrics such as resolution, as well as quantifying image artifacts such as sidelobes and grating lobes.

The geometry of a GPR system using 2-D SAR processing is illustrated in Fig. 1 (for down-looking GPR) and Fig. 2 (for side-looking GPR), which show all the parameters relevant to the analysis performed here. The down-looking configuration assumes that the linear synthetic aperture passes directly above the buried target. Since we do not know the target location a priori, this particular geometry is only seldom encountered in practice. In fact, in the most common scenarios, the radar operates in a side-looking configuration, with various lateral aperture offsets with respect to the target position. Nevertheless, investigating the down-looking geometry for GPR systems is of major interest, as a limit case in a continuum of aperture offsets for side-looking configurations.

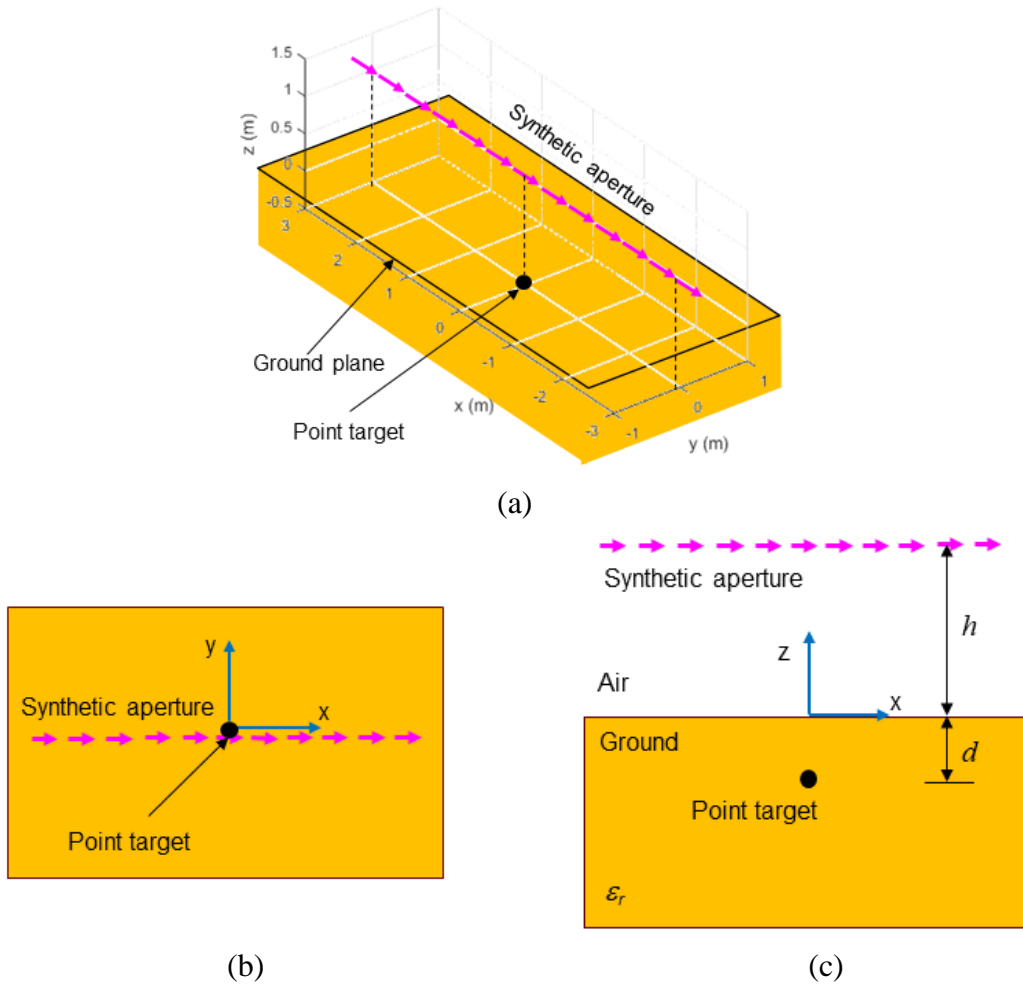


Fig. 1 Schematic representation of the GPR SAR system using a linear synthetic aperture in down-looking configuration: a) perspective view; b) top view; c) side view

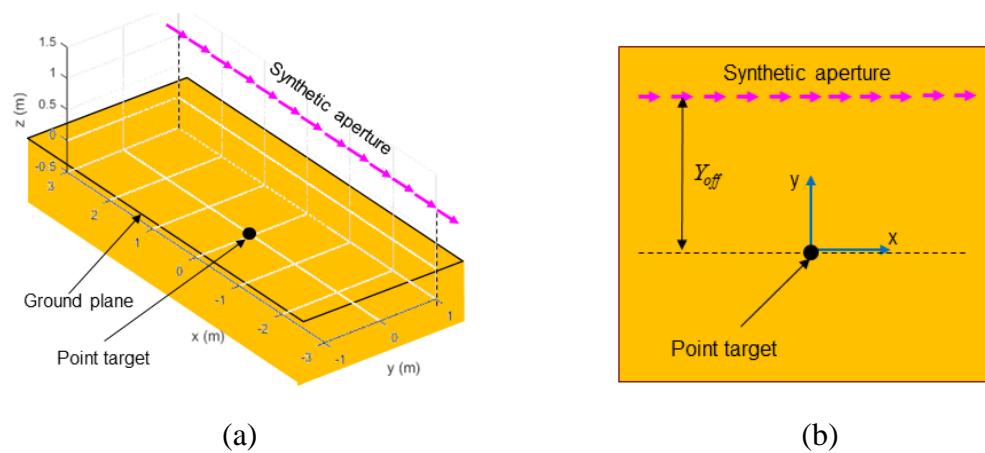


Fig. 2 Schematic representation of the GPR SAR system using a linear synthetic aperture in side-looking configuration: a) perspective view; b) top view

The antennas are modeled as small dipoles, with orientations along the x axis (or along-track) for the horizontal-horizontal (H-H) polarization and along the z axis for the vertical-vertical (V-V) polarization. Throughout this report, we only consider monostatic radar configurations, with the Tx and Rx antennas collocated at each aperture sample position.

In this section, we also list the equations relevant to the PSF and SAR image calculations performed in the remainder of this report. These equations were derived in Part I of this study.¹ The PTR for H-H and V-V polarizations, obtained at frequency f_l , with the radar positioned at $\mathbf{r}_m = [x_m \ y_m \ h]^T$ and the target placed at $\mathbf{r}_0 = [x_0 \ y_0 \ -d]^T$, is given by

$$\text{PTR}_{HH}(f_l, \mathbf{r}_m, \mathbf{r}_0) = (A_{\phi x}^2(f_l, \mathbf{r}_m, \mathbf{r}_0) + A_{\theta x}^2(f_l, \mathbf{r}_m, \mathbf{r}_0)) \exp\left(-j \frac{4\pi f_l}{c} R_m\right), \quad (1a)$$

$$\text{PTR}_{VV}(f_l, \mathbf{r}_m, \mathbf{r}_0) = A_{\theta z}^2(f_l, \mathbf{r}_m, \mathbf{r}_0) \exp\left(-j \frac{4\pi f_l}{c} R_m\right), \quad (1b)$$

where

$$A_{\phi x} = \frac{k_0}{\rho} \frac{\sin \phi \sin \theta \cos \theta}{\cos \theta + \sqrt{\varepsilon_r' - \sin^2 \theta}} \exp\left(-\frac{k_0 \varepsilon_r'' d}{2\sqrt{\varepsilon_r' - \sin^2 \theta}}\right), \quad (2a)$$

$$A_{\theta x} = \frac{k_0}{\rho} \frac{\sqrt{\varepsilon_r'} \cos \phi \sin \theta \cos^2 \theta}{\varepsilon_r' \cos \theta + \sqrt{\varepsilon_r' - \sin^2 \theta}} \exp\left(-\frac{k_0 \varepsilon_r'' d}{2\sqrt{\varepsilon_r' - \sin^2 \theta}}\right), \quad (2b)$$

$$A_{\theta z} = \frac{k_0}{\rho} \frac{\sqrt{\varepsilon_r'} \sin^2 \theta \cos \theta}{\varepsilon_r' \cos \theta + \sqrt{\varepsilon_r' - \sin^2 \theta}} \exp\left(-\frac{k_0 \varepsilon_r'' d}{2\sqrt{\varepsilon_r' - \sin^2 \theta}}\right). \quad (2c)$$

In these equations, we used the following notations: $k_0 = \frac{2\pi f_l}{c} = 2\pi f_l \sqrt{\varepsilon_0 \mu_0}$ for the free-space wavenumber; $\varepsilon_r = \varepsilon_r' - j\varepsilon_r''$ for the complex dielectric constant of the ground; $\phi = \tan^{-1} \frac{y_m - y_0}{x_m - x_0}$; $\rho = \sqrt{(x_m - x_0)^2 + (y_m - y_0)^2}$; θ for the elevation angle of propagation in the air; and $R_m = \rho \sin \theta + h \cos \theta + d \sqrt{\varepsilon_r' - \sin^2 \theta}$. Note that the validity of these equations is limited to the low-loss dielectric ground case, when the loss tangent² $\tan \delta = \frac{\varepsilon_r''}{\varepsilon_r'}$ is on the order of 0.1.

The SAR imaging algorithm is based on the matched filter method.³ The complex amplitude of the image voxel at position \mathbf{r} is computed as

$$I(\mathbf{r}) = \frac{1}{LM} \sum_{l=1}^L \sum_{m=1}^M W(f_l, \mathbf{r}_m) P(f_l, \mathbf{r}_m) \exp\left(j \frac{4\pi f_l}{c} R_m\right), \quad (3)$$

where l and m are the frequency and aperture sample indexes, respectively, $P(f_l, \mathbf{r}_m)$ is the radar received signal at frequency f_l and aperture position \mathbf{r}_m , and $W(f_l, \mathbf{r}_m)$ is a window function depending on the same parameters. Most of the numerical examples in the following sections of this report use a Hanning window in the frequency domain and a flat-amplitude window for the aperture samples.

When formulating the algorithm in Eq. 3, we considered only the PTR phase in setting the matched filter's transfer function. Alternatives to this imaging procedure, discussed by Dogaru,¹ consist of taking either the conjugate or the inverse of the PTR (magnitude and phase in both cases) as the matched filter's transfer function. The imaging algorithm in these two cases can be formulated as

$$I(\mathbf{r}) = \frac{1}{LM} \sum_{l=1}^L \sum_{m=1}^M P(f_l, \mathbf{r}_m) \text{PTR}^*(f_l, \mathbf{r}_m, \mathbf{r}) \quad (4)$$

or

$$I(\mathbf{r}) = \frac{1}{LM} \sum_{l=1}^L \sum_{m=1}^M P(f_l, \mathbf{r}_m) \frac{1}{\text{PTR}(f_l, \mathbf{r}_m, \mathbf{r})}. \quad (5)$$

To obtain the PSF of the SAR system for a point target placed at \mathbf{r}_0 , we replace $P(f_l, \mathbf{r}_m)$ by $\text{PTR}(f_l, \mathbf{r}_m, \mathbf{r}_0)$ in Eq. 3, which yields the following formula:

$$\text{PSF}(\mathbf{r}, \mathbf{r}_0) = \frac{1}{LM} \sum_{l=1}^L \sum_{m=1}^M W(f_l, \mathbf{r}_m) \text{PTR}(f_l, \mathbf{r}_m, \mathbf{r}_0) \exp\left(j \frac{4\pi f_l}{c} R_m\right). \quad (6)$$

3. PSF Analysis of a 2-D GPR SAR System

3.1 Numeric Examples of PSF for 2-D GPR

Section 3 of this report is dedicated to the analysis of a 2-D GPR system using a linear synthetic aperture, as described in Figs. 1 and 2. We begin with some numerical examples of the PSF meant to illustrate and explain the differences between down-looking and side-looking configurations, as well as between H-H and V-V polarizations.

The SAR images throughout this report are always created as 3-D volumes, even when the synthetic aperture geometry only allows resolving the target in two dimensions. The reason for doing that is twofold: 1) we do not know a priori in which vertical plane the target is located, so simply creating an image in one of these planes could miss the target entirely; and 2) the 3-D volume displays may suggest techniques for resolving the target in all three dimensions, as shown in Section 5. The 3-D images are represented graphically as planar sections through the image volume. The voxel magnitudes are displayed by pseudo-colors in dB scale, with a 40-dB dynamic range. The absolute magnitude values are not important in these images; however, the relative magnitudes between various configurations are preserved to allow a meaningful comparison in terms of performance metrics. Note that all configurations use excitation by dipoles with the same moment magnitude, which is another way of saying that they transmit the same power.

The following parameters are used in creating the images in this section:

- Center frequency $f_0 = 1.25$ GHz
- Bandwidth $B = 1.5$ GHz, from 0.5 to 2 GHz
- Synthetic aperture length $L = 10$ m
- Radar platform height $h = 1$ m
- Lateral aperture offset (for side-looking) $Y_{off} = 1.5$ m
- Point target coordinates: $x_0 = 0$, $y_0 = 0$, and $d = 0.1$ m
- Number of samples in frequency $L = 151$, spaced 10 MHz apart
- Number of aperture samples $M = 101$, spaced 10 cm apart (in x direction)
- Complex dielectric constant of ground $\epsilon_r = 5 - j0.3$

Figure 3 displays the PSF obtained in down-looking configuration with H-H polarization. The most striking feature in these images is the strong ground bounce, which appears to almost merge with the target image in Fig. 3d. This illustrates the main problem with this configuration, namely the fact that the strong ground bounce can interfere with the detection of shallow buried targets. Mitigating this issue can be done by designing an imaging system with very good depth resolution (which requires large signal bandwidth) and/or by employing ground bounce reduction signal processing algorithms, which are outside the scope of this work.

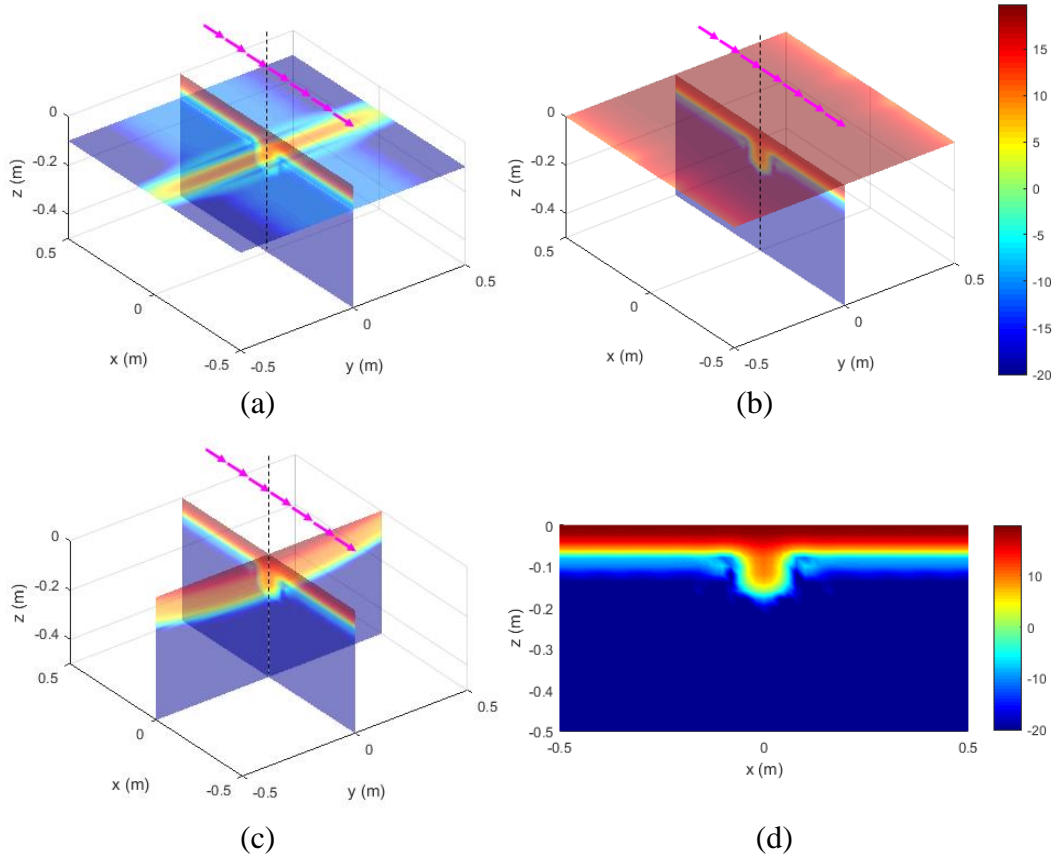


Fig. 3 Graphic representation of the PSF for the GPR system operating in down-looking configuration and H-H polarization, with the point target placed at $x_0 = 0$, $y_0 = 0$, and $d = 0.1$ m: a) $z = -0.1$ m and x-z planes, perspective view; b) $z = 0$ and x-z planes, perspective view; c) x-z and y-z planes, perspective view; d) x-z plane. The SAR images in this figure include the ground bounce.

It is also interesting to display the PSF for the same sensing geometry and polarization, but excluding the ground bounce from the image. This way, we can directly evaluate the point target image without interference from the air-ground interface reflection. This is shown in Fig. 4, which demonstrates that the down-looking geometry with H-H polarization provides very good image resolution in both x and z directions, low sidelobes, as well as the most efficient coupling of the antenna radiated power with the buried target. At the same time, these images have no resolution in the y direction, which was expected given the aperture geometry.

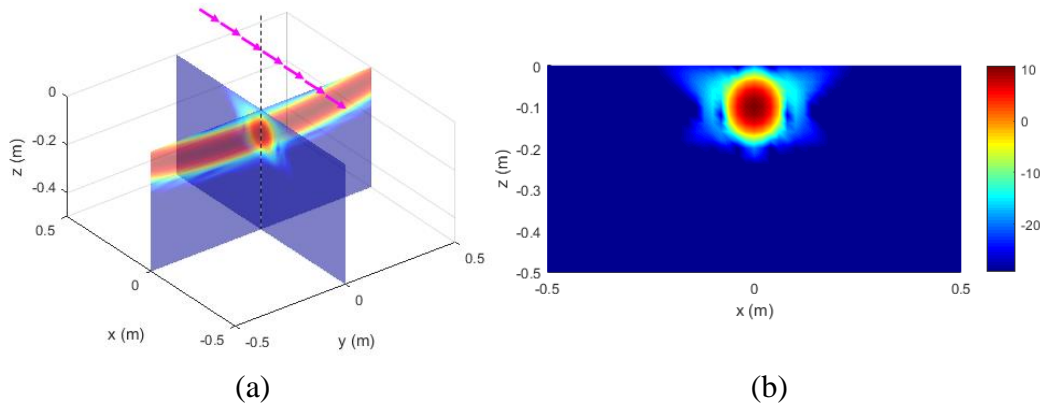


Fig. 4 Graphic representation of the PSF for the GPR system operating in down-looking configuration and H-H polarization, with the point target placed at $x_0 = 0$, $y_0 = 0$, and $d = 0.1$ m: a) x-z and y-z planes, perspective view; b) x-z plane. The SAR images in this figure do not include the ground bounce.

Figures 5 and 6 display the same type of PSF images as Figs. 3 and 4, respectively, this time for down-looking configuration and V-V polarization. The major difference from H-H polarization is the much weaker ground bounce magnitude, which was previously explained by the differences in dipole antenna patterns. As a consequence, the target is readily visible in Fig. 5d, which includes the ground bounce as well. However, one obvious drawback of these images are the large sidelobes, which clearly distort the point target image, as seen in Fig. 6b. Additionally, the magnitude of the PSF is smaller for V-V than for H-H polarization (for down-looking configuration), making the former more susceptible to noise as compared to the latter.

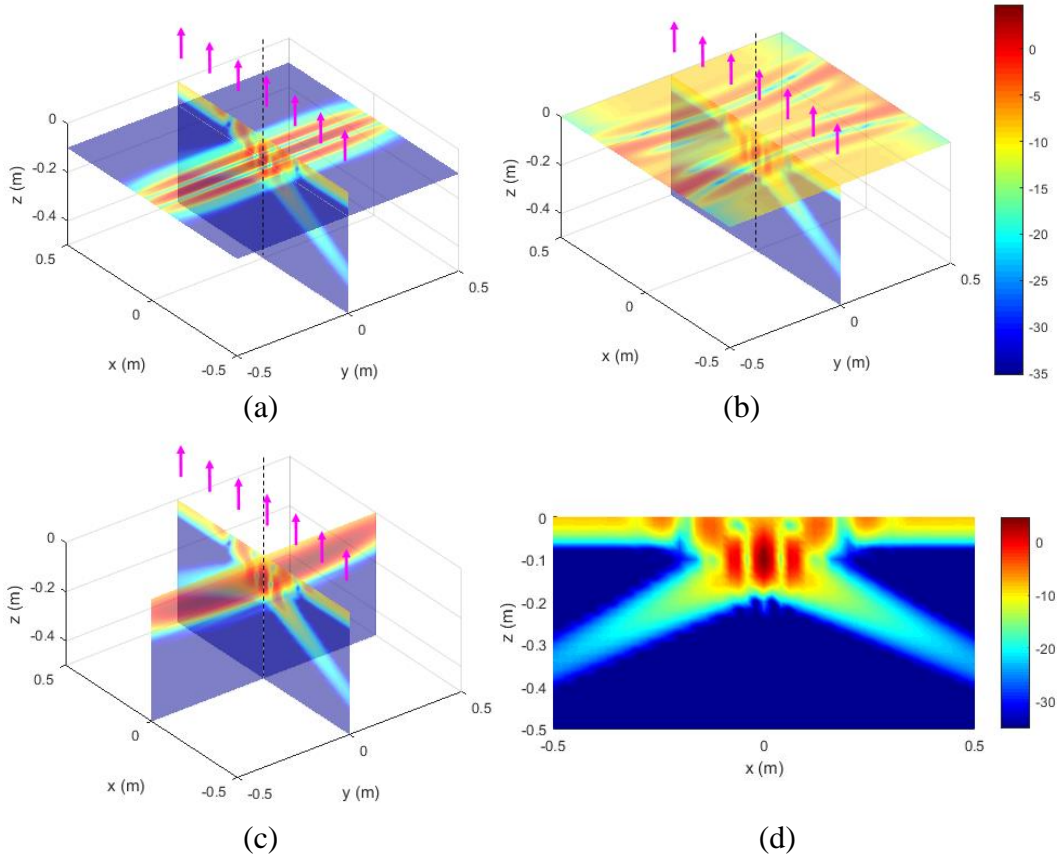


Fig. 5 Graphic representation of the PSF for the GPR system operating in down-looking configuration and V-V polarization, with the point target placed at $x_0 = 0$, $y_0 = 0$, and $d = 0.1$ m: a) $z = -0.1$ m and x-z planes, perspective view; b) $z = 0$ and x-z planes, perspective view; c) x-z and y-z planes, perspective view; d) x-z plane. The SAR images in this figure include the ground bounce.

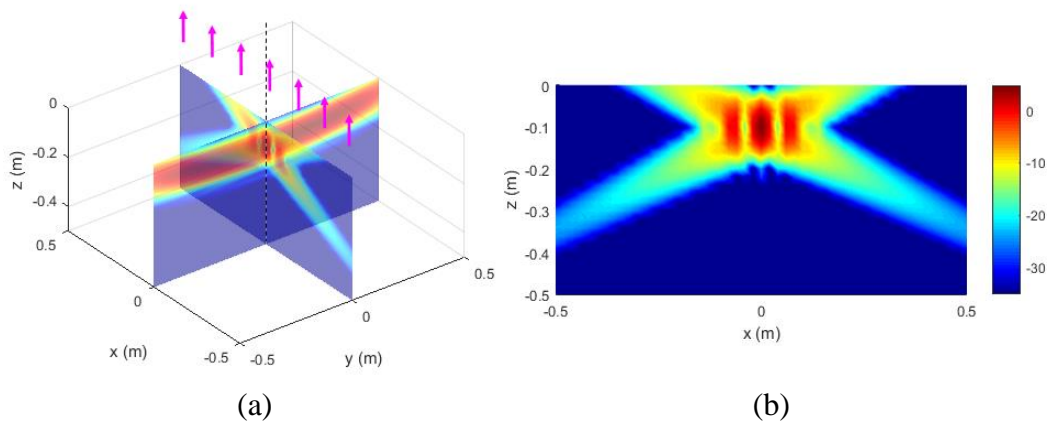


Fig. 6 Graphic representation of the PSF for the GPR system operating in down-looking configuration and V-V polarization, with the point target placed at $x_0 = 0$, $y_0 = 0$, and $d = 0.1$ m: a) x-z and y-z planes, perspective view; b) x-z plane. The SAR images in this figure do not include the ground bounce.

The PSF for side-looking configurations is represented in Figs. 7 and 8, for H-H and V-V polarizations, respectively. The most important departure from the down-looking images is the absence of the ground bounce from the image frame. Note that these ground bounces still exist, but they are pushed outside the limits of the image volume represented in these figures. Therefore, the images in the x - z plane (which contains the point target) are entirely free of ground bounce. This is a great advantage over the down-looking images, since it avoids the need for any ground reflection-mitigation post-processing. Note that there is a slight loss of resolution with respect to the down-looking images (this is discussed in more detail in Section 3.2) and that the side-looking, V-V image displays larger sidelobes than its H-H counterpart. In terms of magnitude, the PSF for side-looking configuration is about the same between the two polarization combinations, and significantly lower than in the down-looking H-H case.

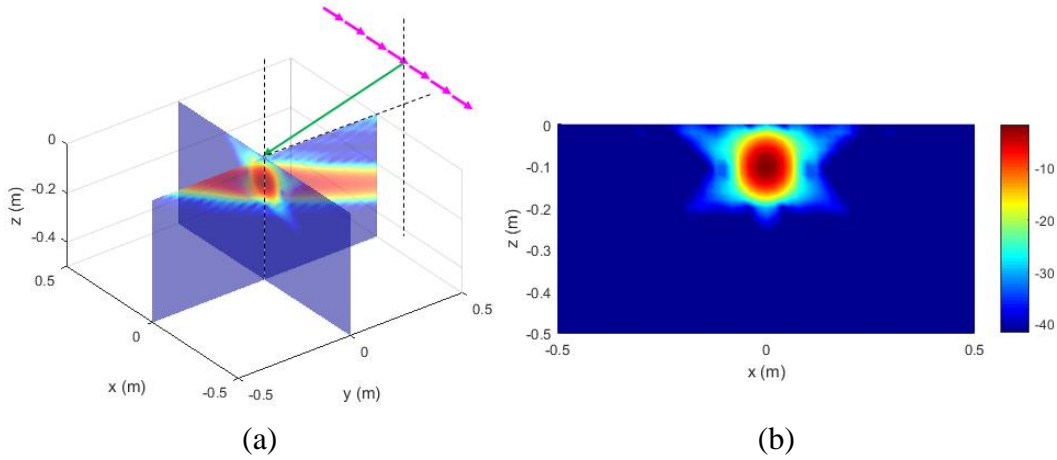


Fig. 7 Graphic representation of the PSF for the GPR system operating in side-looking configuration and H-H polarization, with the point target placed at $x_0 = 0, y_0 = 0$, and $d = 0.1$ m: a) x - z and y - z planes, perspective view; b) x - z plane

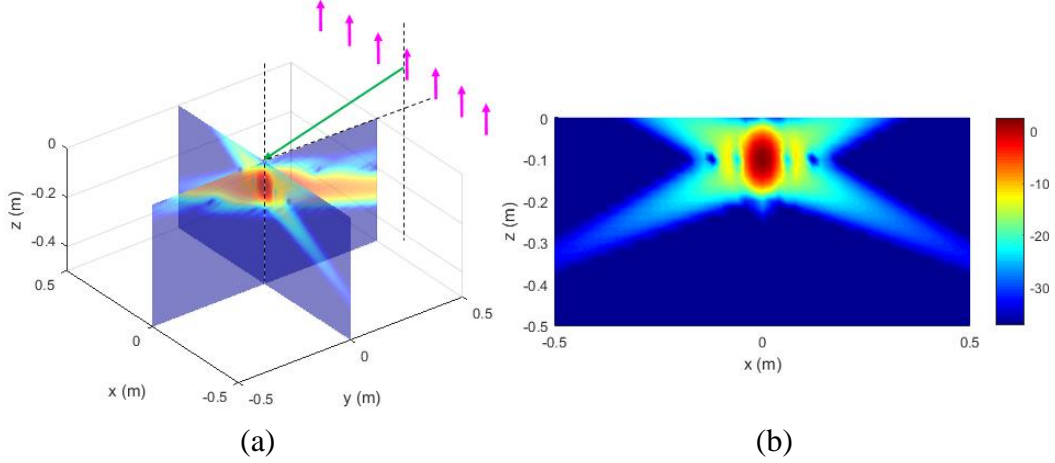


Fig. 8 Graphic representation of the PSF for the GPR system operating in side-looking configuration and V-V polarization, with the point target placed at $x_0 = 0$, $y_0 = 0$, and $d = 0.1$ m: a) x-z and y-z planes, perspective view; b) x-z plane

To understand the differences between various image properties obtained in the four modalities, it helps to compare the amplitude of the radar samples received along the synthetic aperture in each case. These amplitudes are basically given by the quantities $A_{\phi_x}^2 + A_{\theta_x}^2$ (for x-directed dipoles) and $A_{\theta_z}^2$ (for z-directed dipoles), discussed in Section 2. The plots are shown in Fig. 9, for dipoles with x, y, and z orientation, respectively, at the center frequency of the radar signal spectrum (1.25 GHz). (Note: for the y-directed dipole we used $A_{\phi_y}^2 + A_{\theta_y}^2$, which were not given explicitly in Section 2, but can be derived by a procedure similar to the other components.)

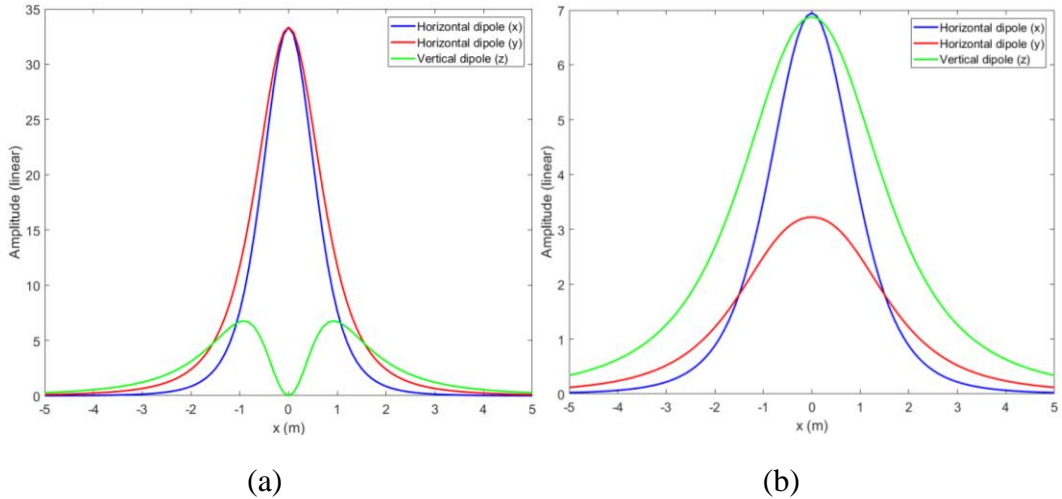


Fig. 9 The aperture amplitude taper function characterizing the GPR system for various dipole antenna orientations in a) down-looking configuration; b) side-looking configuration with $Y_{off} = 1.5$ m. In both cases, the antennas are placed at $h = 1$ m and the frequency is 1.25 GHz.

Note that, except for the z -directed dipole in down-looking configuration, the signal amplitude along the aperture follows a bell-shaped curve. This type of variation, large in the middle of the aperture and tapered towards the ends, is ideal for creating images with low sidelobes. Importantly, the imaging algorithm did not use any additional window in the aperture dimension of the radar data; such a window is not necessary, given the natural taper of the radar data along the aperture.

The z -directed dipole in down-looking configuration generates a different signal amplitude variation along the aperture, with a null right in its middle (remember that a more exact analysis dictates the signal in the aperture's middle be not exactly null, but very small). This type of amplitude variation is the cause of the large sidelobes manifested in the image in Fig. 6b. Some residual sidelobes are also visible in Fig. 8b, for side-looking configuration, z -directed dipole. These can be explained by the fact that the amplitude taper in Fig. 9b (green curve) is not as strong as for the other dipole orientations.

While the signal amplitude taper along the aperture is generally good for suppressing the image sidelobes, it usually comes at the price of a reduction in cross-range resolution when compared to a hypothetical flat amplitude scenario. A quantitative evaluation of this effect is presented in Section 3.2. Another important feature of the graphs in Fig. 9 is the large signal amplitude achieved by the horizontal dipoles in down-looking configuration, relative to all the other cases, which is consistent with the magnitude peaks in the images in Figs. 3–8. This can be explained by differences in antenna patterns (when compared to V-V polarization in down-looking configuration) and by the shorter ranges when compared to the side-looking configurations. An additional comment can be made regarding the similar variation of the radar signal along the aperture for the x - and y -directed dipoles. This suggests that, when equipped with horizontally polarized dipole-like antennas, the system's PSF is not very sensitive to the dipole orientation in the x - y plane and explains our choice to investigate only the x -directed dipole case.

To justify the formulation of the imaging algorithm in Section 2 (Eq. 3), we performed additional simulations by using the matched filter method described by Eq. 4 and the inverse filter method described by Eq. 5. In these images we used the same parameters as before, with down-looking configuration and H-H polarization. The results, shown in Fig. 10, demonstrate the issues with both these methods. Thus, in the matched filter method, the signal amplitude weights along the aperture become squared, which creates an even stronger taper than that displayed in Fig. 9. The effect is a widening of the PSF due to loss of cross-range resolution (Fig. 10a). Conversely, for the inverse filter method, the signal amplitude along the aperture becomes flat, which leads to very strong sidelobes as shown in Fig. 10b. If, in

In addition, we included noise and clutter in the inverse filter method simulation, these would be strongly amplified at the image voxels with weak scattering responses, leading to further degradation in image quality.

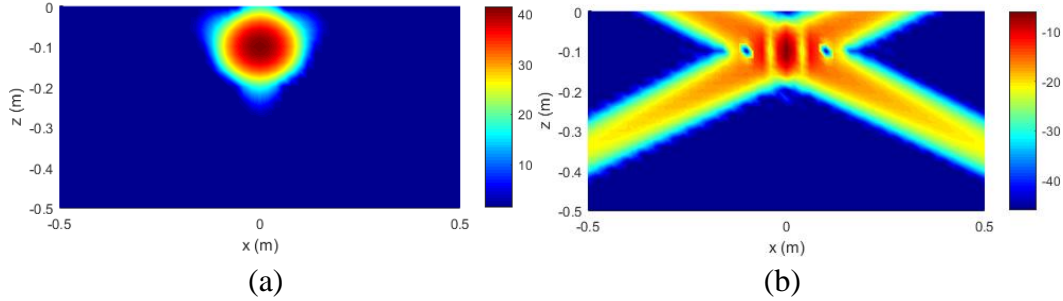


Fig. 10 Graphic representation in the x - z plane of the PSF for the GPR system operating in down-looking configuration and H-H polarization: a) image formed by the matched filter method described by Eq. 4; b) image formed by the inverse filter method described by Eq. 5

Improvements to the conventional imaging algorithm described by Eq. 3 can be made if we introduce an amplitude window in the aperture dimension. This would typically be done to control the image sidelobe levels. An example of this procedure is shown in Fig. 11, for the side-looking configuration, V-V polarizations, where we introduced a Hanning window for the aperture samples. The PSF image in Fig. 11b clearly displays reduced sidelobe levels as compared to those in Fig. 8b. Note that a similar procedure would not be able to improve the sidelobes for the down-looking, V-V polarization case. Moreover, applying a tapered window to any of the H-H polarization scenarios does not make sense, since the natural aperture taper of the radar signal is already strong enough to suppress the image sidelobes to a small level. Nevertheless, the imaging examples presented in this section demonstrate that increased flexibility and better performance can be achieved by employing the algorithm described by Eq. 3 (including the aperture window function) than by using the transfer functions in Eqs. 4 or 5.

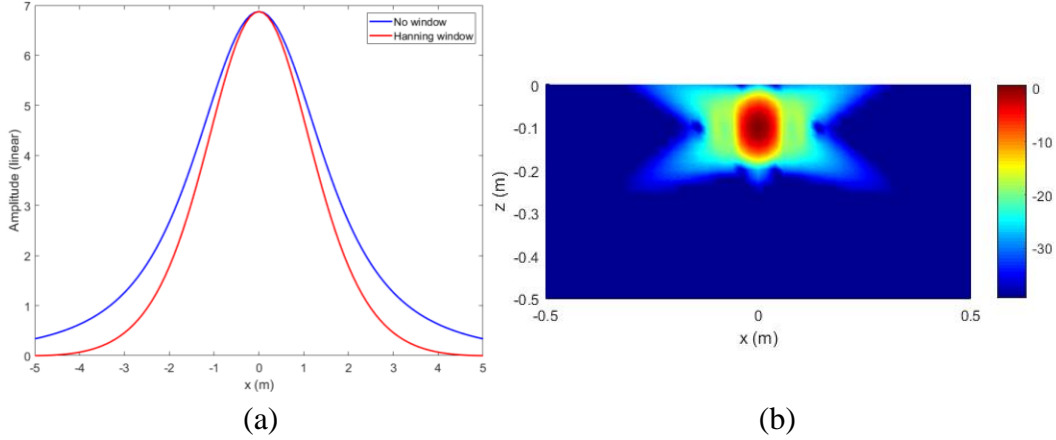


Fig. 11 Illustration of using a Hanning window for aperture tapering for the GPR system operating in side-looking configuration and V-V polarization: a) aperture amplitude taper function with and without the window at 1.25 GHz; b) PSF in the x-z plane

A summary of this section’s findings regarding the GPR system performance for various sensing geometries and polarizations is provided in Table 1. In this table we employ the usual color coding where green means “good”, red means “poor”, and yellow means “in between”. Besides ground bounce, resolution, sidelobes and signal strength, we also considered the robustness to rough surface clutter when evaluating the system’s performance attributes. The latter cannot be investigated by the PSF analysis presented in this section; instead, we used the results in Section 4, based on AFDTD simulations, to evaluate this attribute.

Table 1 Comparison of various GPR imaging system performance attributes between down-looking and side-looking configurations, H-H and V-V polarizations

Attribute	Down-looking H-H	Down-looking V-V	Side-looking H-H	Side-looking V-V
Ground bounce suppression	Red	Yellow	Green	Green
Resolution	Green	Green	Yellow	Yellow
Sidelobes	Green	Red	Green	Yellow
Signal strength	Green	Yellow	Yellow	Yellow
Surface clutter sensitivity	Green	Red	Green	Yellow

3.2 Image Resolution

In this section we perform a quantitative evaluation of the imaging system resolution. Typically, the image resolution analysis of a SAR system is based on the extent of the radar data support in the k -space³ and relies on the assumptions that the radar system and imaging area are in the far-field zone of each other, while

the radar sample magnitudes are approximately constant along the synthetic aperture. However, the GPR sensing scenarios considered in this report present major departures from the traditional SAR model: 1) the imaging area is in the near-field of the radar antennas; and 2) we operate in a half-space environment, where EM propagation effects (such as wave refraction) have a significant impact on system resolution. Consequently, the radar signal magnitude variations along the synthetic aperture cannot be ignored, but must be an integral part of the analysis.

As a result of these departures from the traditional SAR model, many of the textbook-based resolution formulas are not rigorously valid for the GPR configurations considered in this report (the same caveat applies to the grating lobe analysis in Section 3.3). In our case, the exact evaluation of system resolution can only be obtained via numeric simulations. Nevertheless, the analytic results presented here are good approximations, as confirmed by the numerical examples in this section. They are informative to the radar designer as they indicate the system parameters that can be used as performance improvement levers.

All the geometrical parameters relevant to the resolution calculations for the GPR SAR system are shown in Fig. 12. To start the analysis, we first assume that all the radar data samples used in Eq. 3 have equal magnitudes.

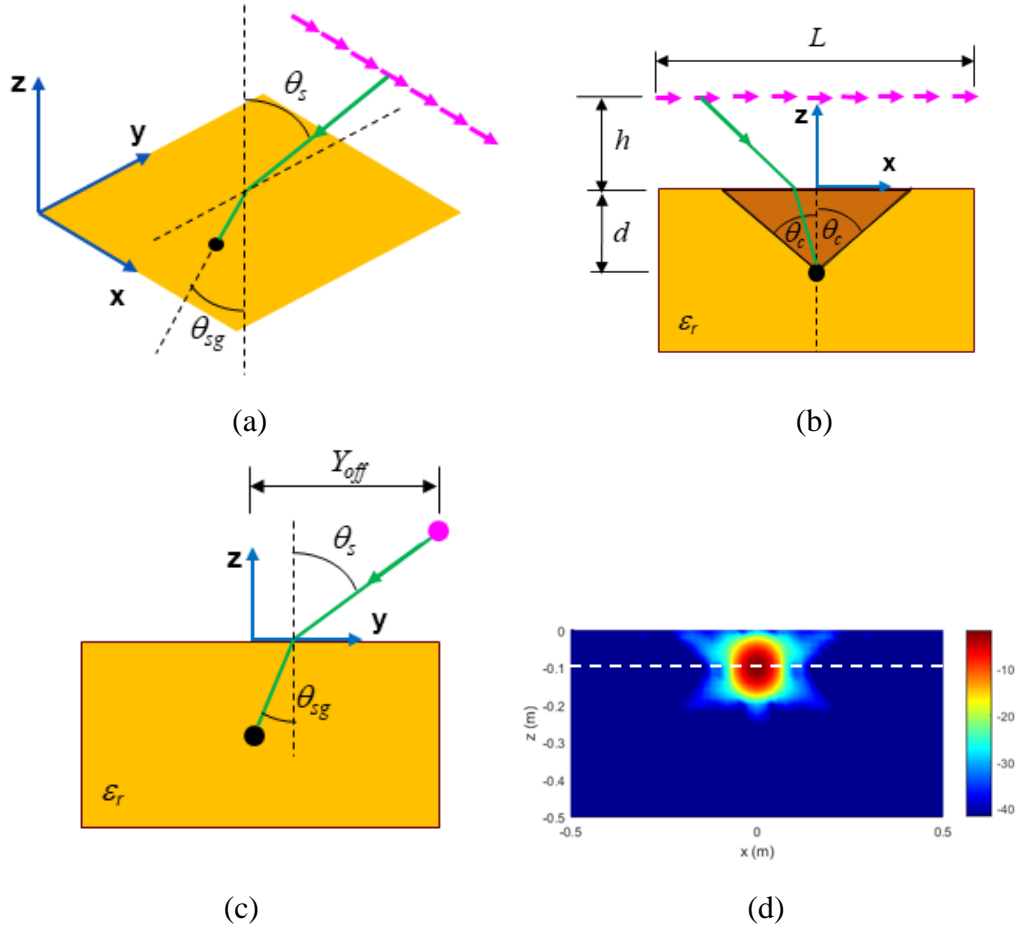


Fig. 12 Geometry of the GPR SAR system showing the parameters relevant to the resolution calculations: a) perspective view; b) side view along the y axis; c) side view along the x axis; d) image example in the x - z plane, showing the white dashed line along which the PSF is evaluated

We start with the resolution in the z direction. For a down-looking GPR, this coincides with the down-range direction, for which the resolution is given by the classic formula $\frac{c}{2B\sqrt{\epsilon_r}}$, where B is the radar signal bandwidth. Notice the $\sqrt{\epsilon_r}$ in the denominator accounting for the slowing of the wave velocity by that factor inside the dielectric ground. (Throughout Section 3 we neglect the imaginary part of ϵ_r and consider it a real number.) For a more general geometry, which includes the side-looking configuration, we need to account for the slant angle θ_{sg} of the propagation path with respect to the imaging plane. Then, the z -direction resolution becomes

$$\delta z = \frac{c}{2B\sqrt{\epsilon_r} \cos \theta_{sg}} . \quad (7)$$

Based on the geometry depicted in Fig. 12c and Snell's law,² the factor in the denominator can be written as

$$\sqrt{\varepsilon_r} \cos \theta_{sg} \cong \sqrt{\varepsilon_r - \frac{Y_{off}^2}{Y_{off}^2 + h^2}} . \quad (8)$$

The last formula is only an approximation, based on the fact that the lateral (y -directed) propagation distance inside the ground is much shorter than the portion above the ground, so we can write $\tan \theta_s \cong \frac{Y_{off}}{h}$. Note that the angles θ_s and θ_{sg} are measured in a plane parallel to the y - z plane, and perpendicular to the synthetic aperture.

To evaluate the resolution in the x direction, we start with the down-looking configuration and make the observation that the aperture integration angle can never exceed two times the critical angle² θ_c (this integration angle is shown as a darker shade in Fig. 12b). The critical angle for an air-dielectric half-space is given by $\theta_c = \sin^{-1} \frac{1}{\sqrt{\varepsilon_r}}$. When ε_r is large enough, we can approximate the arcsine

function by its argument and write $\theta_c \cong \frac{1}{\sqrt{\varepsilon_r}}$. As a numerical example, if ε_r is larger

than 4, θ_c never exceeds 30° , which means the accuracy involved by this approximation is adequate. Given all these considerations, we can formulate the x -directed resolution limit for down-looking GPR as

$$\delta x = \frac{\lambda_0}{4\theta_c \sqrt{\varepsilon_r}} \cong \frac{\lambda_0}{4} , \quad (9)$$

where λ_0 is the wavelength in air, at the center frequency of the radar signal. In the side-looking configuration we need to account for the slant plane imaging geometry. In this case, the cross-range resolution is dictated by the integration angle in the slant plane, which is smaller than $2\theta_c$ by the factor $\cos \theta_{sg}$. Therefore,

$$\delta x = \frac{\lambda_0}{4\theta_c \sqrt{\varepsilon_r} \cos \theta_{sg}} . \quad (10)$$

The important thing to notice when we compare the resolutions of down-looking and side-looking GPR SAR systems is that the slant geometry factor $\cos \theta_{sg}$ is typically close to 1, meaning that the resolution penalty we pay for the side-looking geometry is very small. Indeed, since θ_{sg} can never exceed θ_c , the minimum value for this factor is

$$\left(\cos \theta_{sg}\right)_{\min} = \sqrt{1 - \sin^2 \theta_c} = \sqrt{\frac{\epsilon_r - 1}{\epsilon_r}}. \quad (11)$$

Again, for ϵ_r larger than 4, this number is close to 1 (for example, if $\epsilon_r = 5$, as considered throughout this report, then $\left(\cos \theta_{sg}\right)_{\min} = 0.89$). This fact is further demonstrated by the numerical examples in Fig. 13, where we look at the normalized image magnitude along the white dashed line in Fig. 12d as a function of the lateral aperture offset Y_{off} . In those simulations, the polarization is H-H and all the other parameters are identical with those employed in Section 3.1. The graphs in Fig. 13 show a widening of the PSF main lobe of no more than about 12% (using the down-looking configuration as reference) as we increase the aperture offset. Similar results hold when examining the resolution in the z direction as a function of Y_{off} .

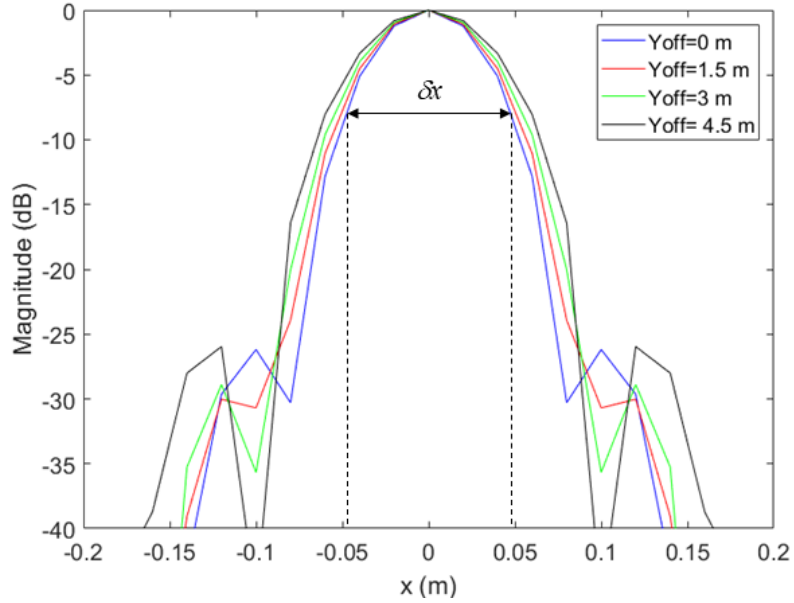


Fig. 13 Main lobe of the PSF showing the cross-range resolution δx (half-width of the lobe) as a function of the lateral aperture offset Y_{off}

Another interesting aspect analyzed in this section is the minimum aperture length needed to reach the x direction resolution limit in Eq. 10. As a reminder, the resolution formulas established so far assumed that all radar data samples (denoted as $P(f_l, \mathbf{r}_m)$ in Eq. 3) have equal magnitudes. However, the graphs in Fig. 9 clearly show that in practice this is not the case. In fact, only a limited number of aperture samples have a significant contribution to the formation of each image voxel; these samples are centered about the x coordinate of the voxel. The effect of the uneven magnitudes of radar samples along the aperture is similar to that of multiplying the flat-magnitude data by a tapered window, which leads to a loss of cross-range

resolution. At the same time, it is apparent that moving the aperture samples far away from the voxel location yields very small increases in the θ propagation angle inside the ground (which is limited by θ_c), meaning that increasing the aperture length past a certain amount has minimal impact on the integration angle dictating the cross-range resolution.

Given all these arguments, we expect that as we increase the aperture length the cross-range resolution tends to a limit value. This resolution limit is about 1.5 to 1.8 times larger than the number predicted by Eq. 9 or 10, which assumed equal magnitudes of the radar samples (the exact resolution degradation factor depends on the shape of the amplitude variation along the aperture). For the down-looking geometry discussed in Section 3.1 and H-H polarization we obtain the theoretical limit $\delta x = 6$ cm (according to Eq. 9). Numerical simulations of the PSF with the same parameters and variable aperture length yield the results in Fig. 14a, where the resolution limit (half-width of the main lobe) is about 9 cm. This limit is reached for (approximately) $L = 2.2$ m. For the side-looking case with $Y_{off} = 3$ m we obtain the graphs in Fig. 14b, where an aperture length $L = 7$ m is needed to reach the resolution limit, which in this case is approximately 10 cm. Using a combination of geometrical considerations and empirical results, we can establish the following approximate formula for the minimum aperture length that attains the cross-resolution limit:

$$L_{min} \cong 2\sqrt{h^2 + Y_{off}^2} + \frac{2d}{\sqrt{\epsilon_r - 1}} . \quad (12)$$

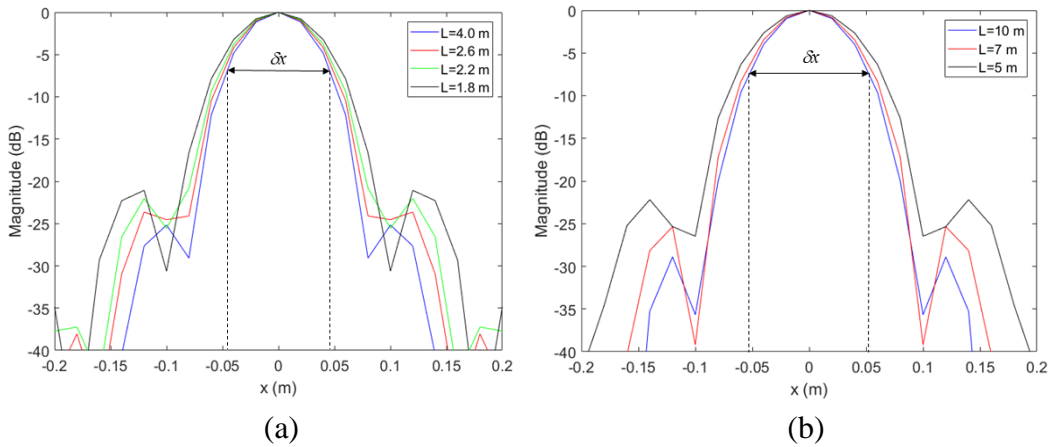


Fig. 14 Main lobe of the PSF showing the cross-range resolution δx (half-width of the lobe) as a function of the aperture integration length L , for: a) down-looking configuration; b) side-looking configuration with $Y_{off} = 3$ m. In both scenarios we used H-H polarization and $h = 1$ m

Regarding the dependence of various resolution metrics on the radar height, we notice that both resolutions (in the z and x directions) are largely insensitive to this parameter. However, the minimum aperture length given by Eq. 12 varies significantly with h , as well as with Y_{off} , suggesting that smaller values of these two parameters enable reaching the cross-resolution limit with a shorter synthetic aperture.

3.3 Image Grating Lobes

The image grating lobes (also known as ambiguities in the radar literature³) are an artifact of radar signal processing, which manifests itself as false replicas of a target response showing at incorrect spatial locations. In this section, we discuss the grating lobes in the cross-range direction, which have significant impact on the radar system design. One way to ensure the absence of these grating lobes from the radar image is to choose a sample spacing along the synthetic aperture smaller than $\frac{\lambda_{\min}}{4}$, where λ_{\min} corresponds to the highest frequency in the signal spectrum. For the simulations presented in this section, with a maximum frequency of 2 GHz, this corresponds to 3.75 cm.

If the $\frac{\lambda_{\min}}{4}$ sampling criterion cannot be satisfied, the distance between cross-range grating lobes is generally dictated by the radar sample spacing along the synthetic aperture. One basic rule in designing the SAR system parameters is to choose radar data sampling rates that ensure unambiguous ranges larger than the image size in all spatial dimensions. However, this design rule is not entirely applicable to strip-map SAR systems, since the along-track image extent is theoretically infinite (in practice, very large), and any scattering object can create ambiguous responses appearing at the wrong location inside the image volume. When the cross-range grating lobes are present in the image, it is important to understand how to keep them under control and possibly mitigate them.

The classic grating lobe analysis for SAR systems³ is based on certain assumptions, which typically state that either the image cross-range extent or the synthetic aperture length (or both) are much smaller than the aperture-target range. Unfortunately, due to the near-field geometry, these assumptions are not valid for our GPR sensing scenario and therefore analytic expressions for the grating lobe location are not possible. The analysis in the following paragraphs is based on the traditional far-field assumptions employed by most authors. Although these assumptions are not strictly valid in our scenario and the expressions are only approximate, the final results are close to the numeric simulations and can be used as guiding rules in a system design.

The drawing in Fig. 15 helps formulate a relationship between the aperture sampling rate and the distance between cross-range grating lobes. Thus, if the desired grating lobe spacing is D , the angular sampling interval inside the ground must be

$$\Delta\theta_g = \frac{\lambda_g}{2D} = \frac{\lambda_0}{2D\sqrt{\epsilon_r}}, \quad (13)$$

where λ_g is the wavelength in the ground at the center frequency. In the general case, the corresponding aperture sampling interval Δl is

$$\Delta l = \sqrt{h^2 + X_{off}^2 + Y_{off}^2} \Delta\theta \cong \sqrt{h^2 + X_{off}^2 + Y_{off}^2} \Delta\theta_g \sqrt{\epsilon_r} = \sqrt{h^2 + X_{off}^2 + Y_{off}^2} \frac{\lambda_0}{2D}. \quad (14)$$

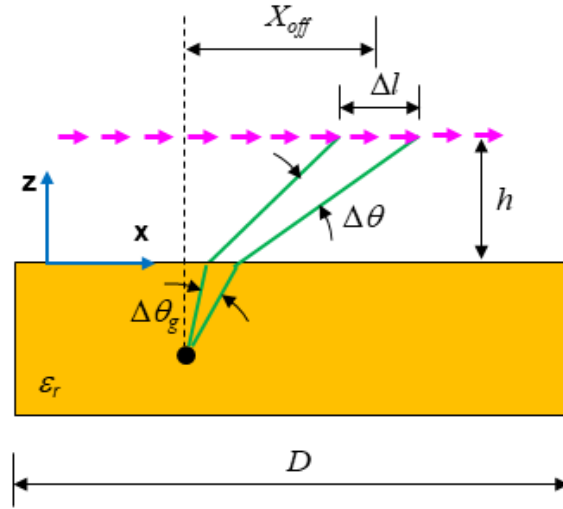


Fig. 15 Geometry of the GPR SAR system showing the parameters used in the calculations related to grating lobe spacing as a function of the aperture sampling rate

The most stringent case (which requires the smallest sampling interval) occurs for aperture samples directly above the target ($X_{off} = Y_{off} = 0$), where we obtain

$$\Delta l = \frac{\lambda_0 h}{2D}. \quad (15)$$

Conversely, given an aperture sampling interval Δl we can find the distance to the first grating lobes as

$$D = \frac{\lambda_0 h}{2\Delta l}. \quad (16)$$

Figure 16 shows a PSF image example that includes the presence of grating lobes. Since $\Delta l = 10$ cm, the grating lobes appear at $D = 1.2$ m from the point target location. Note that this image was obtained for the same parameters as those shown

in Fig. 4 (with ground bounce suppressed). However, the images in Fig. 4 do not exhibit the grating lobes because the image domain was truncated to a cross-range dimension smaller than D .

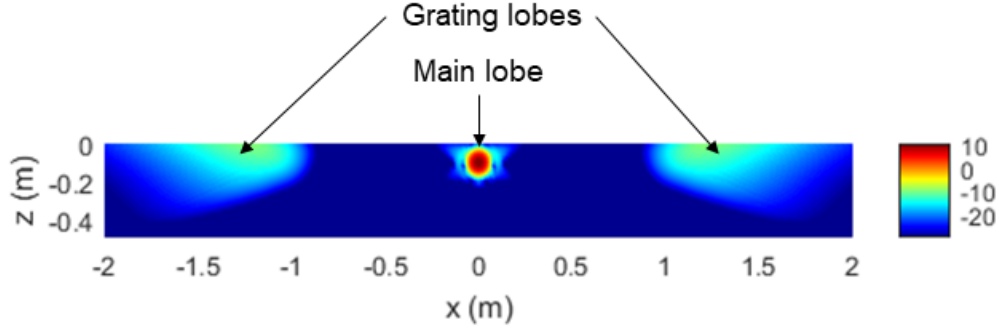


Fig. 16 PSF for the GPR system operating in down-looking configuration and H-H polarization, for the same parameters as in Fig. 4, emphasizing the cross-range grating lobes

An exact analysis of the position and magnitude of the grating lobes for this radar geometry and propagation environment would be very complex and is not attempted in this study. Factors contributing to the difficulty of this analysis are the near-field propagation geometry, the presence of the half-space environment, the non-uniform magnitude of the radar samples along the aperture, and the UWB nature of the radar waveform. Nevertheless, our numerical studies clearly show that increasing the aperture spatial sampling rate both pushes the grating lobes farther away from the target image and reduces their magnitude, to the point of their complete elimination when the $\frac{\lambda_{\min}}{4}$ criterion is met.

As an interesting effect displayed in Fig. 16, the grating lobes appear much more diffuse than the main PSF lobe and their magnitude is about 25 dB below the PSF peak. The grating lobe attenuation can be partially explained by the fact that we use UWB waveforms as radar signals. To qualitatively explain this mechanism, we notice that each frequency sample integrated over the synthetic aperture adds a contribution to the image voxel at the grating lobe location, which has a different phase compared to the contributions at other frequencies. Adding these noncoherent contributions (as complex numbers) results in a voxel magnitude that is clearly below that of the main lobe, where all the contributions add coherently. While a quantitative analysis of this effect has not been yet developed, analogies with the attenuation of Doppler grating lobes for UWB signals⁴ suggest that the attenuation factor is proportional to the fractional bandwidth $\frac{B}{f_0}$.

Going back to Eq. 15, one can infer that for a given grating lobe spacing D , the required aperture sampling interval increases proportionally with the radar

platform's height. In Section 3.2, we established that to reach the cross-range resolution limit, the synthetic aperture length needs to increase with h (in fact, for down-looking configuration, this relationship is linear). Consequently, we can meet both performance metrics (grating lobe spacing and cross-range resolution) with a fixed number of aperture samples, independently of the radar height. This number of samples is (for down-looking geometries)

$$M = \frac{L_{\min}}{\Delta l} \cong \frac{4D}{\lambda_0}. \quad (17)$$

If, on the other hand, we want to obtain a grating-lobe-free image by meeting the $\Delta l = \frac{\lambda_{\min}}{4}$ criterion, then the number of required aperture samples increases with the radar height according to

$$M = \frac{L_{\min}}{\Delta l} \cong \frac{8h}{\lambda_{\min}}. \quad (18)$$

3.4 Impact of Target Depth on GPR Images

All the PSF simulation examples in Section 3.1 assumed a target buried at shallow depth ($d = 0.1$ m). While these models may be relevant to many buried explosive hazard scenarios, it is also interesting to investigate the SAR images of targets buried at larger depths. In this section, we compare the PSF images obtained for $d = 0.1$ m (as in Section 3.1) with those obtained for $d = 0.2$ m. Figure 17 displays both images for down-looking configuration and H-H polarization, with the other parameters identical with those used in Section 3.1. Two immediate conclusions can be drawn by comparing these two images: 1) the deep buried target can be readily separated from the ground bounce (Fig. 17b), while the same cannot be stated for the shallow buried target (Fig. 17a); and 2) the magnitude of the deep target image is significantly lower than that of the shallow target image, due to the longer propagation path coupled with the radar wave attenuation inside the ground.

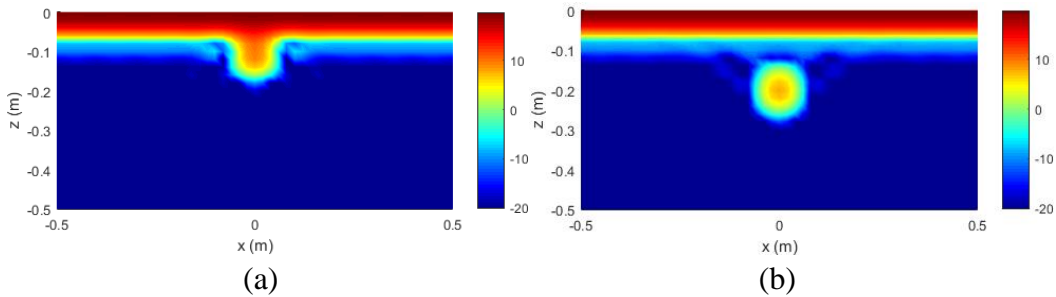


Fig. 17 PSF for the GPR system operating in down-looking configuration and H-H polarization, with the point target buried at a) $d = 0.1$ m and b) $d = 0.2$ m

Additional image comparisons between the two target depths are shown in Fig. 18, where we considered both down-looking and side-looking configurations, and both H-H and V-V polarizations. Note that these images do not include the ground bounce, allowing us to make a clear comparison of the PSF peak magnitude among all the different cases (each image dynamic range is scaled by its own maximum voxel magnitude). For the soil parameters and frequencies considered in this GPR sensing scenario, this magnitude drops by approximately 3 dB when the target depth increases by 10 cm. One should keep in mind that for these simulations we chose a relatively low-loss dielectric soil. Operating the GPR in a soil environment with higher dielectric losses can dramatically reduce the image magnitude of deep buried targets. At the same time, it is apparent from the images in Fig. 18 that the resolution is not significantly impacted by the target burial depth.

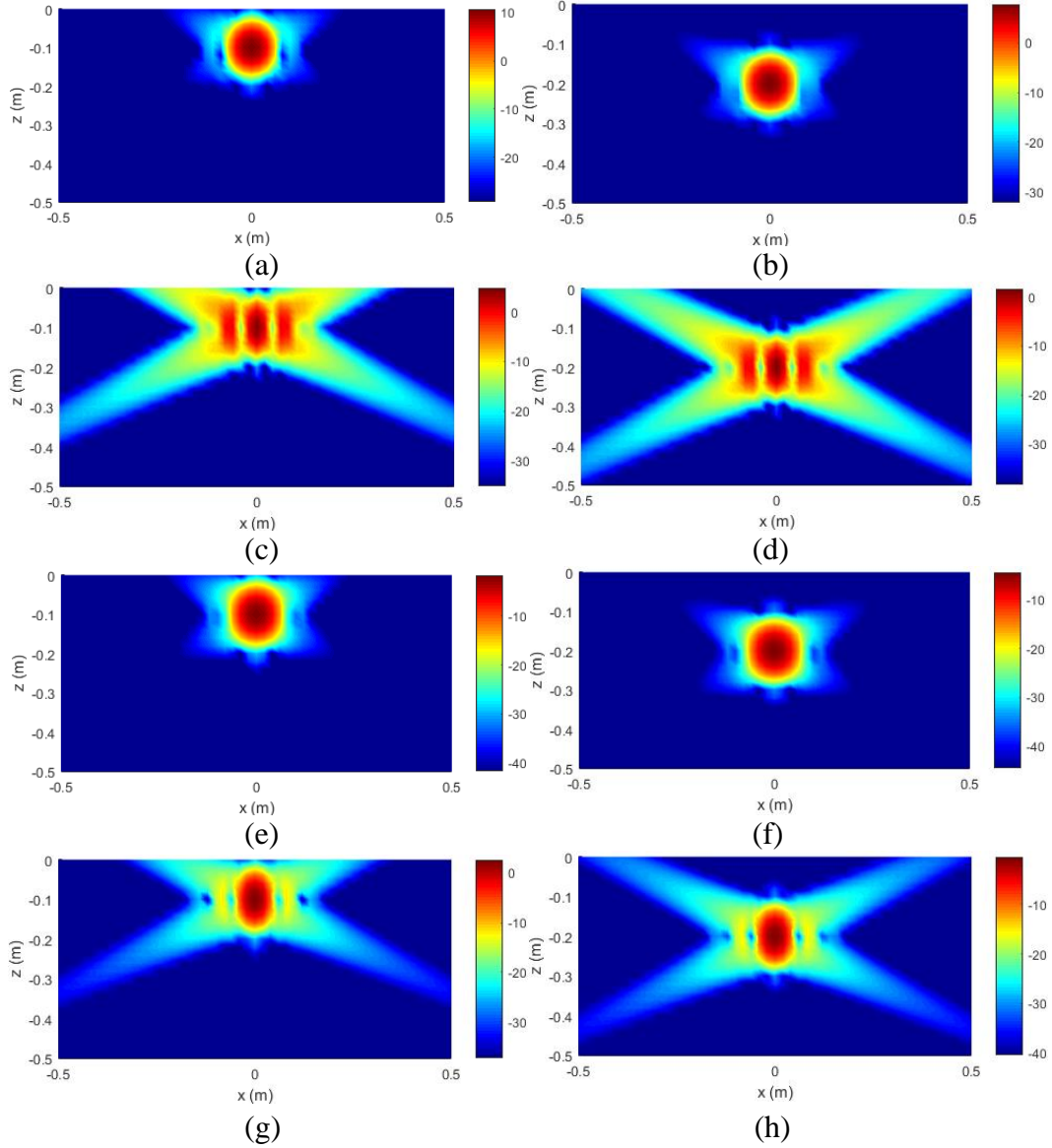


Fig. 18 PSF for the GPR system for the following configurations: a) $d = 0.1$ m, H-H, down-looking; b) $d = 0.2$ m, H-H, down-looking; c) $d = 0.1$ m, V-V, down-looking; d) $d = 0.2$ m, V-V, down-looking; e) $d = 0.1$ m, H-H, side-looking; f) $d = 0.2$ m, H-H, side-looking; g) $d = 0.1$ m, V-V, side-looking; and h) $d = 0.2$ m, V-V, side-looking. The ground bounce was not included in these images.

Based on the images in Figs. 17 and 18, we conclude that the H-H polarization in down-looking configuration seems the most favorable for detection of deep buried targets, especially since the target separation from the ground bounce becomes less of a problem in this case. One caveat to this conclusion is the impact that the combination of strong ground bounce and weak target return has on the radar system's dynamic range. This issue is particularly relevant to a down-looking, H-H-polarized GPR system, which may require a very high dynamic range to detect deep buried targets.

One final comment related to target burial depth concerns the impact of soil inhomogeneities on target detection, which could become significant as the depth increases. Throughout this report, we ignored these effects, as simulation tools for handling them have not yet been developed at the time of this writing. Nevertheless, modeling the presence of soil inhomogeneities in GPR scenarios is a topic deserving more attention that hopefully will be investigated in future work.

3.5 Choice of Frequency and Bandwidth

When choosing the frequencies of the radar waveform for GPR imaging applications, we need to take into account the effectiveness of wave propagation inside the ground, as well as the image resolution. With regard to wave propagation, the attenuation through the soil dielectric medium generally increases with frequency.⁵ Thus, for good penetration, the radar signals should be limited to frequencies below 3 GHz. As for the lower frequency limit, this is generally dictated by the need to keep the radar antenna size within reasonable limits. This is particularly important in designing a compact airborne radar system that can be installed on an sUAV platform. A practical lower limit for radar waveforms typically employed by GPR designers is 300 MHz.

In terms of resolution, the analysis in Section 3.2 shows that good down-range resolution requires large bandwidth, while good cross-range resolution requires large center frequency (or small wavelength). Achieving good down-range (or depth) resolution is critical in situations where we try to spatially separate a shallow buried target from the ground bounce. Thus, 2 GHz of bandwidth allows a depth resolution of about 7.5 cm, which could be enough to separate targets buried at depths as small as 10 cm. However, digitizing signals with large bandwidths typically require fast sampling rates, which are particularly demanding on the analog-to-digital converters (ADCs). Direct sampling of a signal with 2-GHz bandwidth at the Nyquist rate pushes the limits of current ADC technology, and devices achieving this performance are still very expensive. Alternatives to direct sampling of radar signals have been developed for GPR systems to mitigate this issue; examples include stroboscopic sampling of UWB impulses⁶ and stepped-frequency waveforms.⁷

The need for large center frequency to achieve good cross-range resolution is in direct conflict with the ground penetration properties of the radar waves, so a balance must be struck between the two requirements. Based on computer models and the experience of many GPR designers, a good compromise in terms of performance can be obtained with radar waveforms in a spectrum between 0.5 and 2.5 GHz.

To demonstrate the effect of the bandwidth and center frequency on the PSF of a GPR system, we performed some simple simulations on a point target buried at $d = 0.2$ m, in down-looking configuration and H-H polarization, by varying the two parameters. The results are shown in Fig. 19, for frequencies between a) 0.5 and 2.5 GHz; b) 0.5 and 1.5 GHz; and c) 1.5 and 2.5 GHz. The image in Fig. 19b shows a poor separation of the target from the ground bounce, due to the reduced bandwidth, while the image in Fig. 19c displays a visible difference between the down-range and cross-range resolutions (the center frequency is too high relative to the bandwidth). It is apparent that Fig. 19a achieves the most balanced image of the point target; this case is consistent with the frequency spectrum choice stated in the previous paragraph.

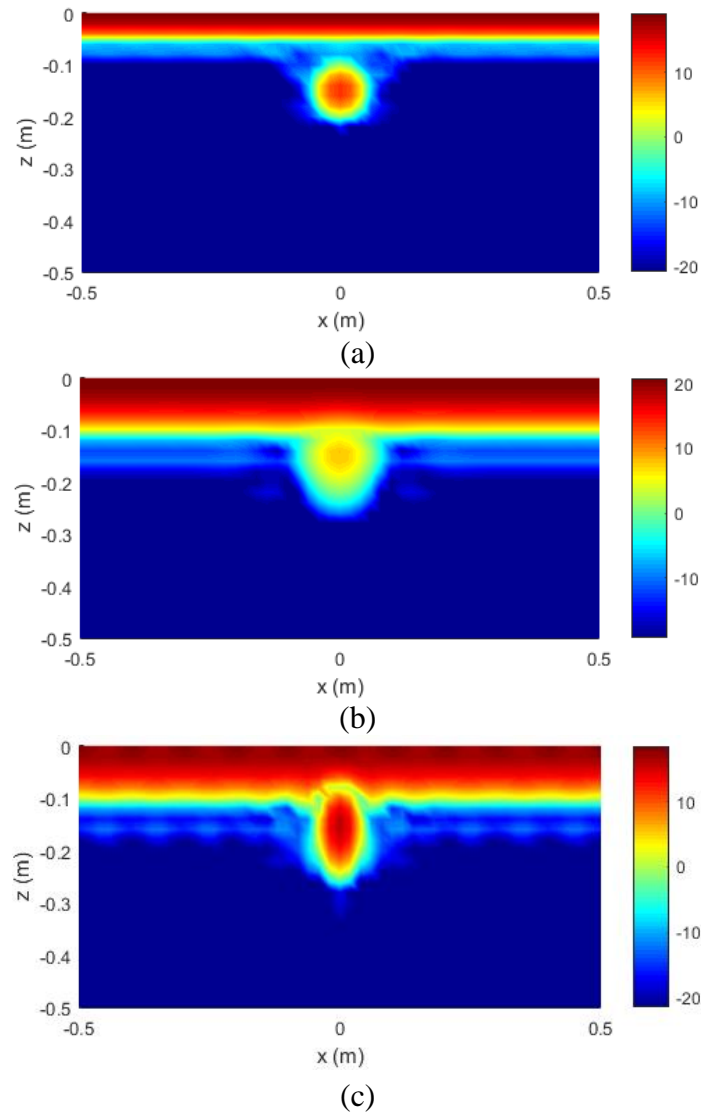


Fig. 19 PSF of the GPR system in down-looking configurations and H-H polarization, with the point target placed at a depth $d = 0.15$ m and operating in the following frequency bands: a) 0.5 to 2.5 GHz; b) 0.5 to 1.5 GHz; c) 1.5 to 2.5 GHz

3.6 Radar Signal Power

Calculations of the radar received power are essential in ensuring that the system provides enough signal-to-noise ratio (SNR) for target detection. In general, GPR systems operate at very short ranges and need very little average power to achieve a satisfactory SNR. Note that the classic radar equation³ cannot be applied directly to a close-to-ground GPR system due to the near-field configuration. A method for computing the required transmitted power for a near-field SAR system, based on computer simulated scattering data, was presented elsewhere.⁸ In this section, we focus on comparing the received power of a GPR system in various sensing geometries, between the H-H and V-V polarizations.

The plots in Fig. 20 show magnitude differences between the radar responses for the two polarizations. This is confirmed by examining the magnitude peaks in the images throughout Section 3.1 (one should only consider the images that exclude the ground bounce). To understand these differences, remember that the point target response magnitude is dictated by the antenna patterns, air-ground transmission coefficient, path loss, and attenuation through the ground, all evaluated for the round trip propagation. Among these factors, only the antenna patterns and the transmission coefficient differ between the two polarizations. In Fig. 20 we show the variation of the amplitude factors (which appear in Eq. 1) with the lateral aperture offset (Y_{off}) at two different positions along the aperture ($x = 0$ and $x = 1$ m).

In Fig. 20a we notice that for small lateral offset (close to the down-looking configuration), the H-H response is much stronger than the V-V response. As we increase the offset past 1.5 m (side-looking configuration), the V-V response becomes larger than the H-H counterpart, but only slightly so. The conclusion drawn from this analysis is that H-H polarization definitely offers larger received power in down-looking configuration, whereas in side-looking configuration, the two polarization combinations perform about the same in terms of radar received power. This statement is reinforced by the results in Fig. 20b.

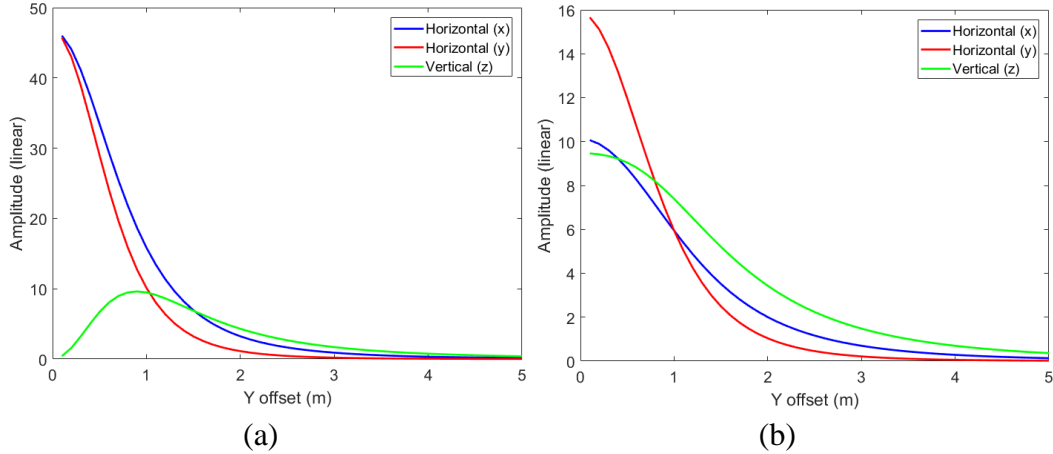


Fig. 20 Graphic representation of the PTR amplitude factor as a function of the y direction aperture offset and various dipole antenna polarizations, at 1.25 GHz, for a) $x = 0$ and b) $x = 1$ m

3.7 Effect of Positioning Errors

The formation of well-focused SAR images requires maintaining the coherence of the collected data over a coherent processing interval. In practice, to accurately measure the radar signal’s phase we need to know the antenna’s phase center coordinates with respect to a ground reference frame, at the slow-time sampling instances, with a precision on the order of a fraction of the wavelength.⁹ In principle, these coordinates can be inferred from the platform’s trajectory, assuming we know its direction of travel, velocity, and acceleration. Additionally, small deviations from the ideal trajectory can be measured by a navigation system such as GPS and fed as motion compensation data into the image formation algorithm. However, insufficient accuracy of the navigation data can lead to residual positioning errors, with negative impact on the SAR imaging process.

In this section we perform computer simulations with the goal of quantifying the effects of platform positioning errors on the SAR image quality and deriving the maximum allowable deviations before the quality degrades to unacceptable levels. Detailed theoretical considerations related to this problem were developed elsewhere¹⁰ and are not repeated in this work. One important conclusion of that previous study was that errors occurring along the line of sight (LOS) have the largest impact on the image formation process, whereas those occurring in a direction perpendicular to the LOS have no influence on the image. Consequently, in the following numerical examples, we only consider platform translational errors in the y and z directions (or across-track errors). To be exact, errors along the x direction (or along-track errors) also have a component along the LOS, but this is significant only for large along-track offsets with respect to the target, where the

radar signal is weak; consequently, these errors are expected to have very little impact on the overall image quality.

The positioning errors along the y and z directions are modeled as zero-mean Gaussian random processes, uncorrelated from one slow-time sample to the next, and uncorrelated between the y and z directions. This represents the worst-case scenario for SAR image formation—introducing correlation between the samples typically lessens the error’s impact on the image. The Gaussian random processes have a standard deviation (or RMS error) that is incremented while we monitor the PSF peak magnitude. The upper RMS limit of the positioning errors is obtained when the peak magnitude drops more than 3 dB below the error-free image peak. Note that if σ_y and σ_z are the RMS errors in the y and z directions, respectively, we measure the overall positioning RMS error as $\sqrt{\sigma_y^2 + \sigma_z^2}$ (this is called the distance root mean square [DRMS] in the GPS-related literature and represents the most commonly referenced performance specification of a GPS system). In our models, we assume $\sigma_y = \sigma_z$ and only list the DRMS under each simulation case.

The simulation results are shown in Figs. 21 and 22, for down-looking and side-looking configurations, respectively (H-H polarization was considered in both cases), with the DRMS increasing from 0 to 4.2 cm, in 1.4 cm increments. The point target is placed at a depth $d = 0.2$ m, while the other parameters are identical to previous simulations in Section 3. The value of the PSF peak magnitude for each scenario is listed in Table 2 (notice that, for the images in Fig. 21, we consider the peak of the target image magnitude, not the overall image peak reached by the ground bounce). The numbers in this table indicate that, for DRMS = 2.8 cm, the peak drops about 3 dB below the error-free case (which is marginally acceptable), while for DRMS = 4.2 cm, this drop is about 6–7 dB (which is clearly unacceptable). The conclusion drawn from this analysis is that the GPR imaging system can tolerate positioning errors with DRMS up to about 3 cm. This figure represents a tenth of a wavelength at 1 GHz, which is in line with general prescriptions for SAR systems. It is also an accuracy level that can be readily achieved by current variants of the GPS technology, such as the real-time kinematic (RTK) systems.¹¹

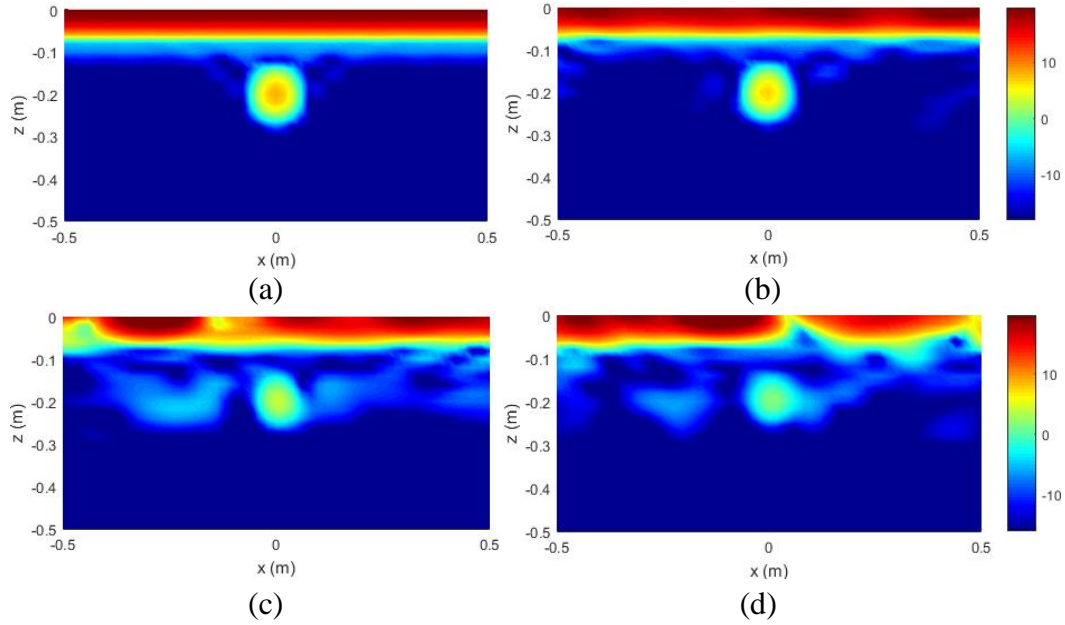


Fig. 21 PSF of the GPR system in down-looking configurations and H-H polarization, with the point target placed at a depth $d = 0.2$ m, before and after introducing positioning errors: a) no errors; b) errors with 1.4-cm RMS; c) errors with 2.8-cm RMS; d) errors with 4.2-cm RMS. Note that all images are scaled to the same maximum voxel magnitude.

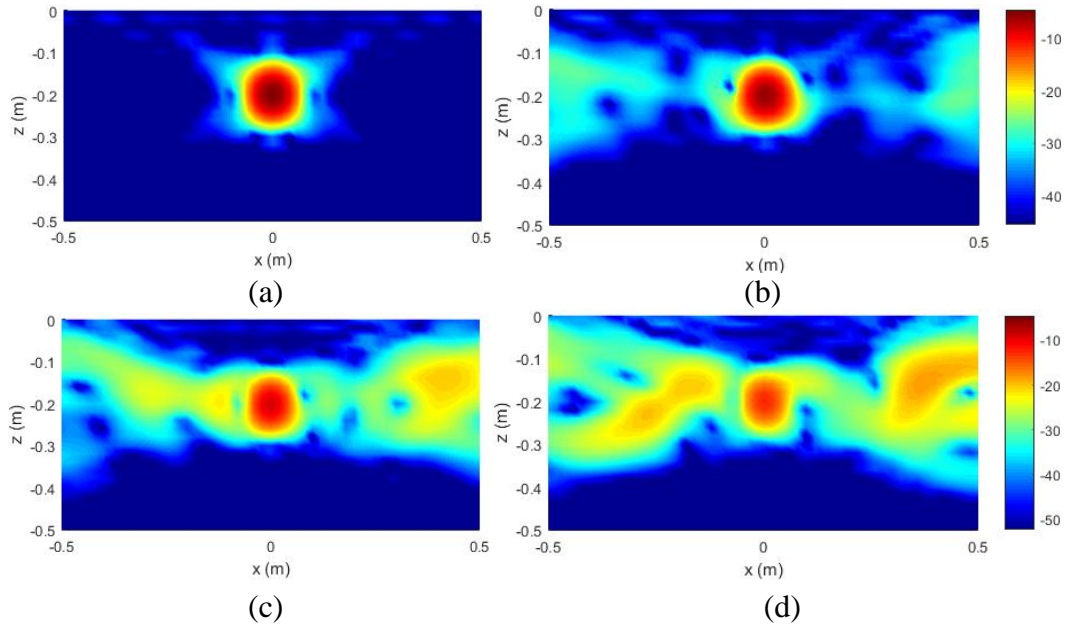


Fig. 22 PSF of the GPR system in side-looking configurations and H-H polarization, with the point target placed at a depth $d = 0.2$ m, before and after introducing positioning errors: a) no errors; b) errors with 1.4-cm RMS; c) errors with 2.8-cm RMS; d) errors with 4.2-cm RMS. Note that all images are scaled to the same maximum voxel magnitude.

Table 2 Peak voxel magnitudes for the PSF images in Figs. 21 and 22, before and after introducing positioning errors

DRMS (cm)	Down-looking (dB)	Side-looking (dB)
0	7.8	-4.5
1.4	6.6	-5.4
2.8	3.6	-8.3
4.2	-0.3	-12.3

4. Modeling GPR SAR Imaging System for Buried Landmines

So far, the GPR system analysis was based on the PSF, which is the image obtained in the presence of an idealized point target. It is of significant interest to model the radar imaging system's performance for more realistic scenarios, using targets commonly encountered in counter-explosive hazard (CEH) applications. For this purpose, the EM modeling team at the US Army Combat Capabilities Development Command Army Research Laboratory has developed powerful simulation tools, capable of handling a wide variety of radar scattering scenarios. In this study, we employ a near-field version of the AFDTD software,¹² based on the finite-difference time-domain (FDTD) method, which was designed specifically for the radar configurations considered in this report. The target used in these simulations is an M15 antitank metallic landmine, which has a relatively large radar signature. This choice is appropriate for the present investigation, where the main focus is on GPR phenomenology, rather than detection performance. The sensing geometry for these simulations is depicted in Fig. 23, with the other radar parameters being identical with those in Section 3.1, with the exception of the aperture length ($L = 4$ m in this case, which is large enough to meet the limit in Eq. 12). As in the PSF simulations, the antennas are modeled as small dipoles, with a length equal to the size of the FDTD cell (in our case, 2 mm). The Tx and Rx dipoles are slightly offset with respect to one another (by 2 cm in the x direction), but they work very close to a monostatic configuration.

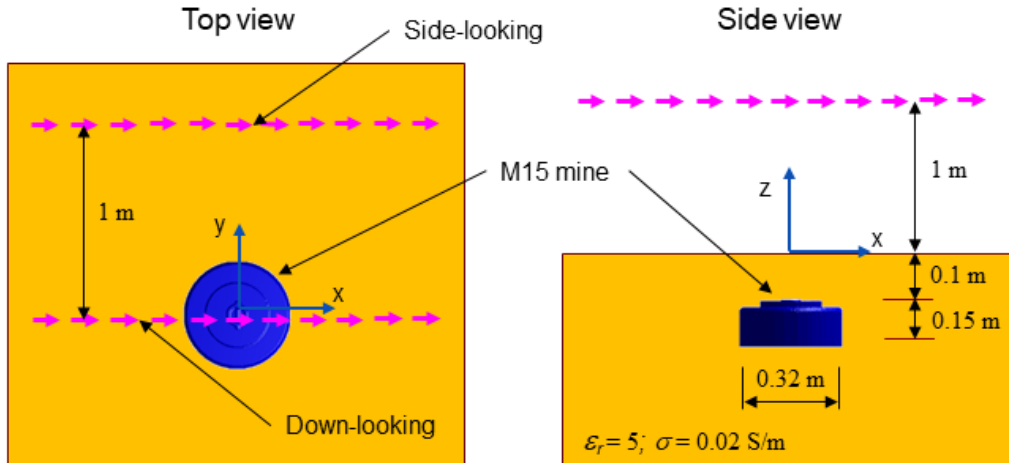


Fig. 23 Representation of the AFDTD modeling geometry used by the GPR SAR system for imaging a buried M15 landmine, showing the top and side views with the relevant dimensions and parameters

The SAR images based on the AFDTD data are created with the algorithm described by Eq. 3 and the graphic representations are similar to those in Section 3.1. Note that in a few cases, we overlaid the target contour onto the radar image to help the interpretation of certain scattering features linked to the target geometry. Also, since the AFDTD software can output scattering data including or excluding the ground bounce, we took advantage of this capability in the radar image analysis.

Figures 24 and 25 represent the images obtained for down-looking configuration and H-H polarization. In Fig. 24, where we included the ground bounce, we notice that this image feature merges with the return from the top of the landmine (the pressure plate), which is an undesired effect. The images in Fig. 25, which exclude the ground bounce, present a cleaner picture of the target scattering phenomenology. Thus, besides the well-localized response from the target's top surface, we notice two other strong returns from the small corners created between the top pressure plate and the rest of the cylindrical case. Additionally, the image displays secondary peaks at depths of 0.25 and 0.35 m, which are the results of multiple reflections between target scattering centers and the air-ground interface. It is apparent that the rich scattering phenomenology coupled with the good image resolution enables isolating several features that could be used in a target identification algorithm.

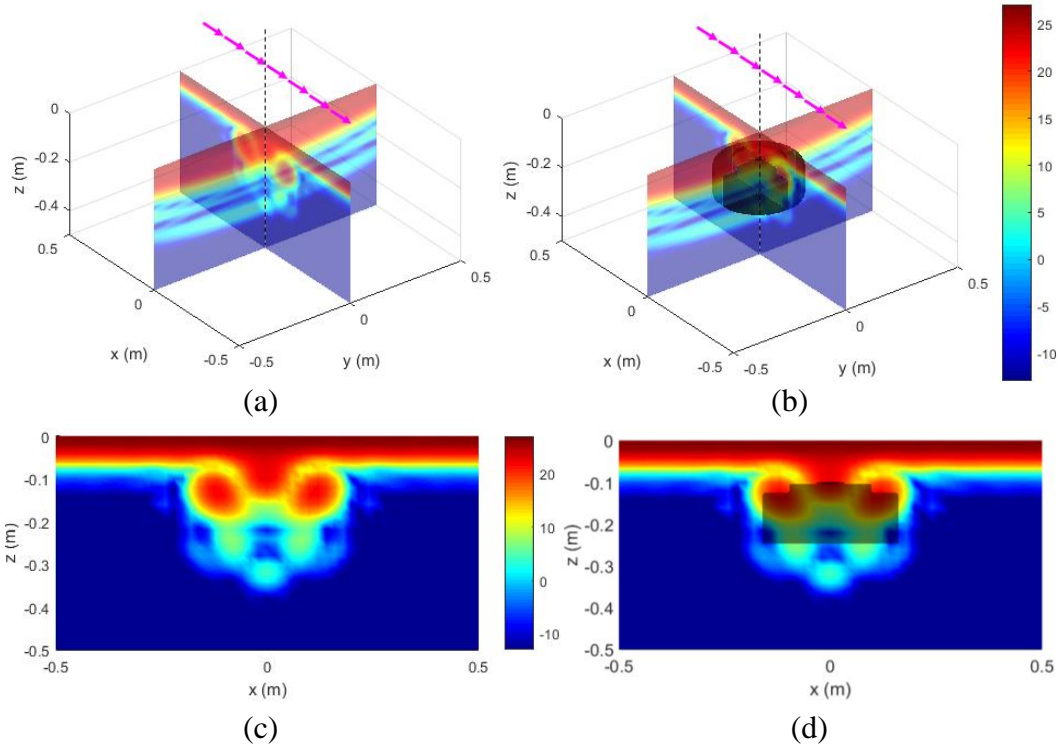


Fig. 24 SAR image of the buried M15 landmine obtained with the GPR system in down-looking configuration and H-H polarization: a) x-z and y-z planes, perspective view; b) same as in a) with target overlay; c) x-z plane; d) same as in c) with target overlay

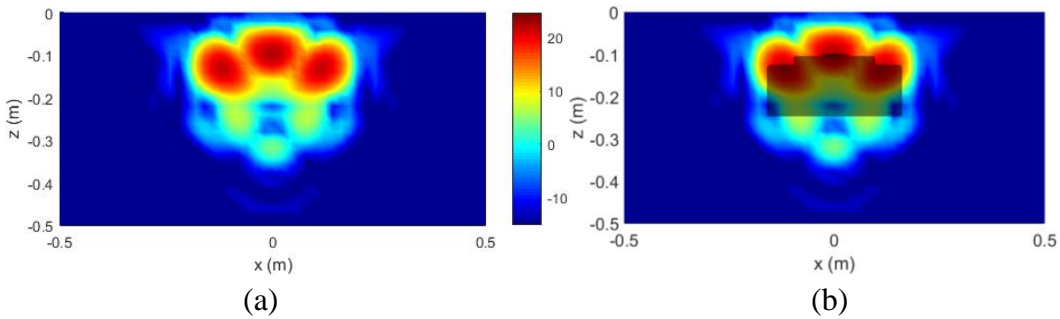


Fig. 25 SAR image of the buried M15 landmine obtained with the GPR system in down-looking configuration and H-H polarization, with the ground bounce removed: a) x-z plane image; b) x-z plane image with target overlay

Figure 26 shows the image obtained for down-looking configuration and V-V polarization. Although the ground bounce is significantly suppressed as compared to the previous case, the high sidelobe levels introduce artificial image features that do not correspond to the real target geometry. For this reason, it is unlikely that this sensing modality would be successfully employed in practical GPR systems.

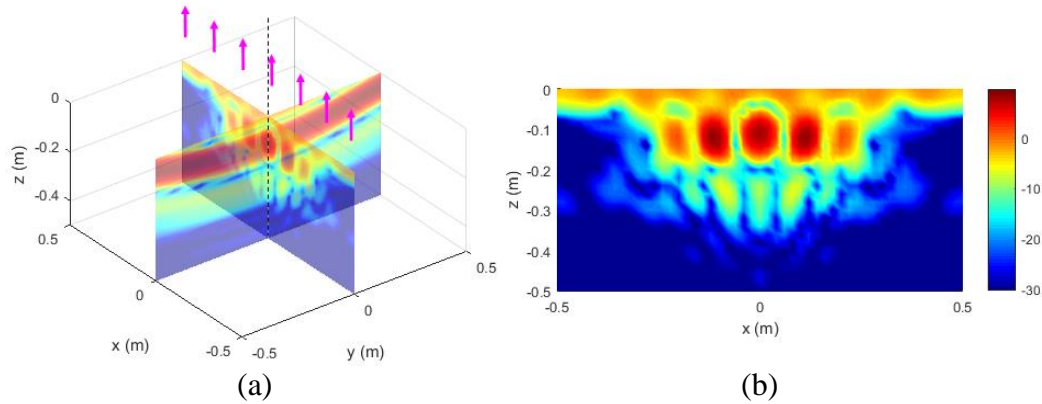
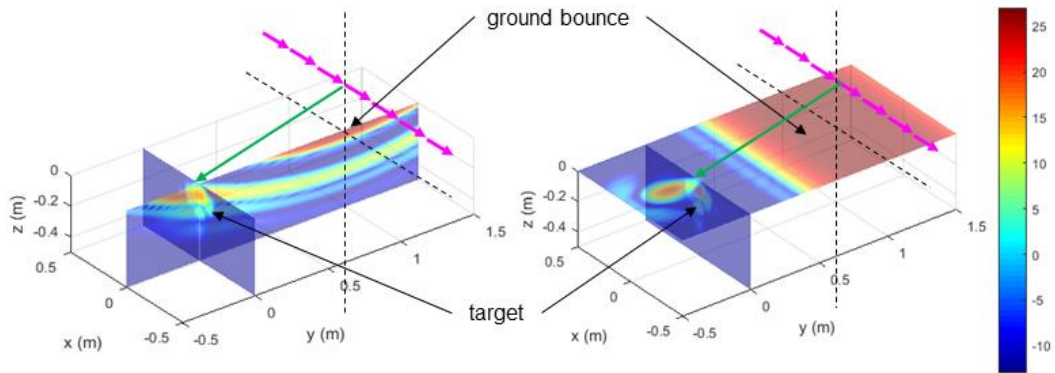


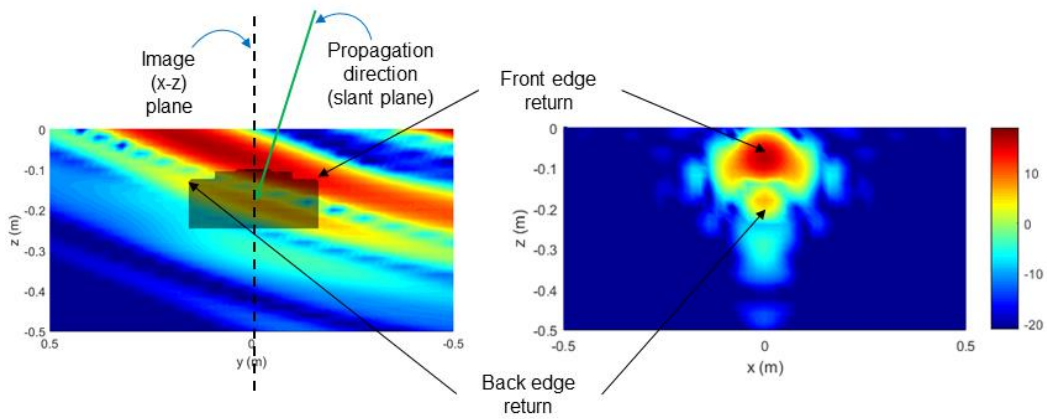
Fig. 26 SAR image of the buried M15 landmine obtained with the GPR system in down-looking configuration and V-V polarization: a) x-z and y-z planes, perspective view; b) x-z plane

The images obtained for side-looking configurations are displayed in Figs. 27 and 28, which include additional details illustrating interesting phenomenological aspects. Thus, in the perspective views (Figs. 27a and 28a), we extended the image frame in the y direction to include the ground bounce, which is mostly focused directly below the synthetic aperture track. These images clearly show the large spatial separation between the target and the ground bounce afforded by the side-looking configuration, which is a positive feature for target detection.

Figures 27b and 28b emphasize the fact that the main scattering centers visible in the side-looking images are produced by edge diffraction phenomena. This can be readily understood by examining the images in the y - z planes, where we used the target overlay to identify the scattering centers. The magnitude ratio between the front and back edge diffraction returns is larger for H-H than for V-V polarization, which is consistent with the geometric theory of diffraction² (note that the dB scales for the two cases have different ranges). Another interesting effect of the side-looking geometry is the absence of multiple target-interface reflections from the SAR images, due to the oblique propagation angle of the radar waves.



(a)



(b)

Fig. 27 SAR image of the buried M15 landmine obtained with the GPR system in side-looking configuration and H-H polarization: a) perspective view; b) y-z and x-z planes, respectively

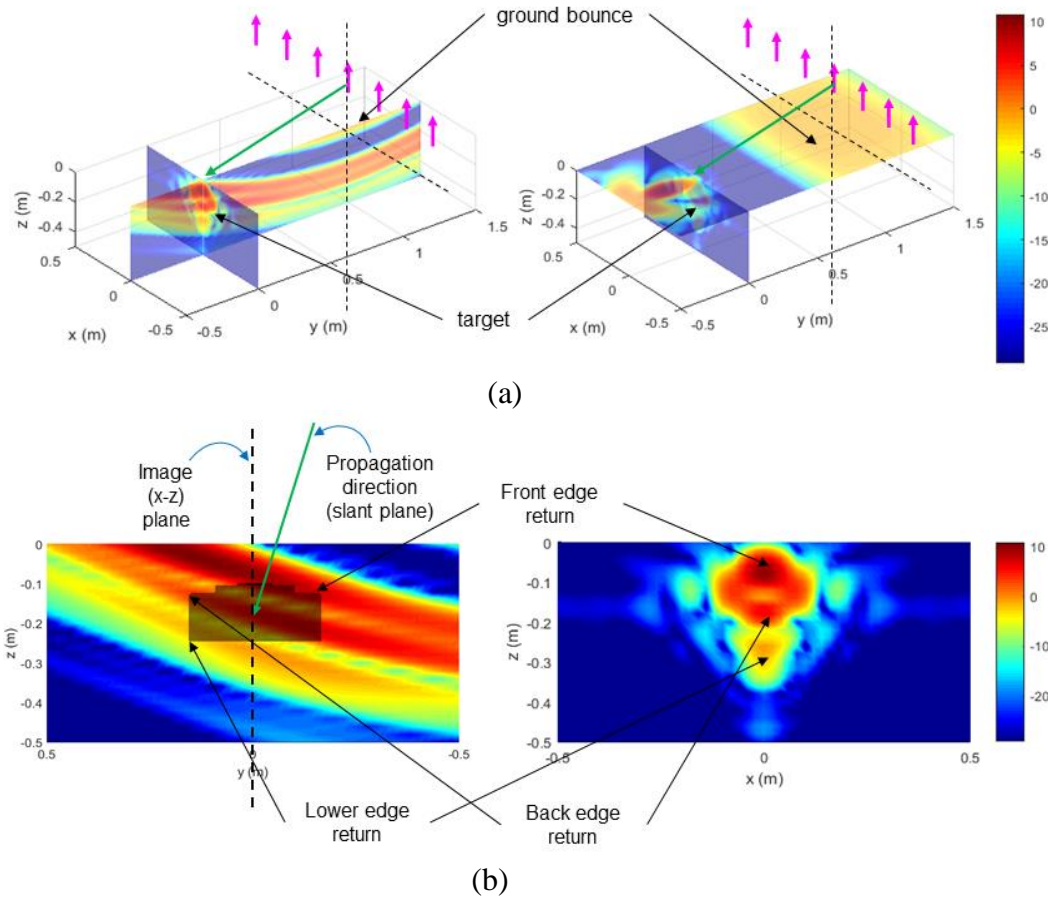


Fig. 28 SAR image of the buried M15 landmine obtained with the GPR system in side-looking configuration and V-V polarization: a) perspective view; b) y-z and x-z planes, respectively

The AFDTD software allows the analysis of buried target scattering in the presence of a rough air-ground interface. For this purpose, we modeled the interface as a 2-D random process with an RMS height of 3 mm and a correlation length of 5 cm. The random process samples are Gaussian-distributed and have an exponential correlation function, independent of azimuth. The surface parameters are consistent with those of a relatively smooth dirt or gravel road.¹³ The remaining figures in this section (Figs. 29–32) represent the M15 images obtained in the presence of the rough surface, for the four sensing modalities analyzed throughout this report. These images display both the presence of a certain amount of clutter in previously “quiet” regions, and a degree of distortion in the target image. It is apparent that the V-V polarization images show larger image distortions under rough surface clutter conditions than their H-H counterparts, with the down-looking, V-V image quality looking particularly poor. Nevertheless, the rough surface simulations indicate no significant loss in terms of peak magnitude of the target image, suggesting that small terrain roughness as considered in these numeric examples does not have large impact on the GPR detection performance.

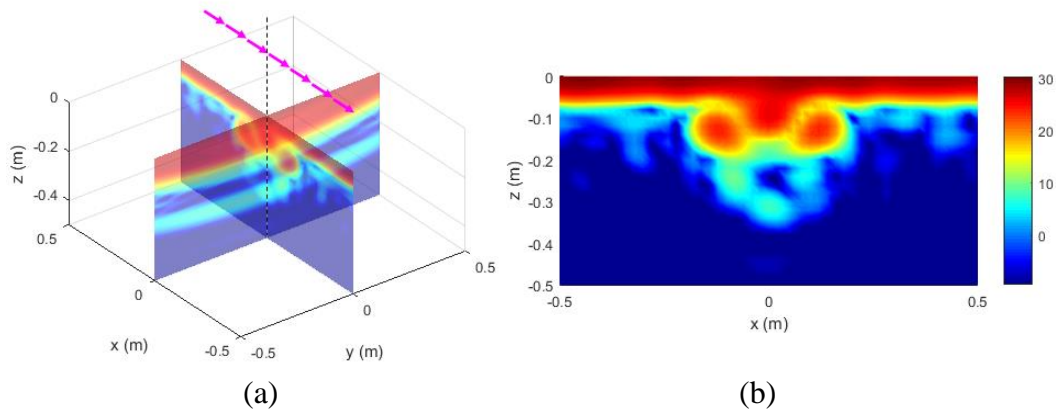


Fig. 29 SAR image of the M15 landmine buried under a rough ground surface obtained with the GPR system in down-looking configuration and H-H polarization: a) x-z and y-z planes, perspective view; b) x-z plane

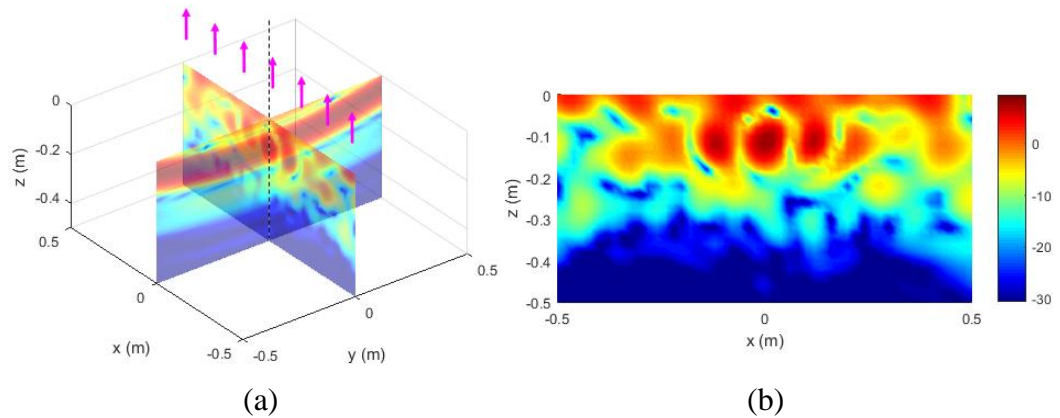


Fig. 30 SAR image of the M15 landmine buried under a rough ground surface obtained with the GPR system in down-looking configuration and V-V polarization: a) x-z and y-z planes, perspective view; b) x-z plane

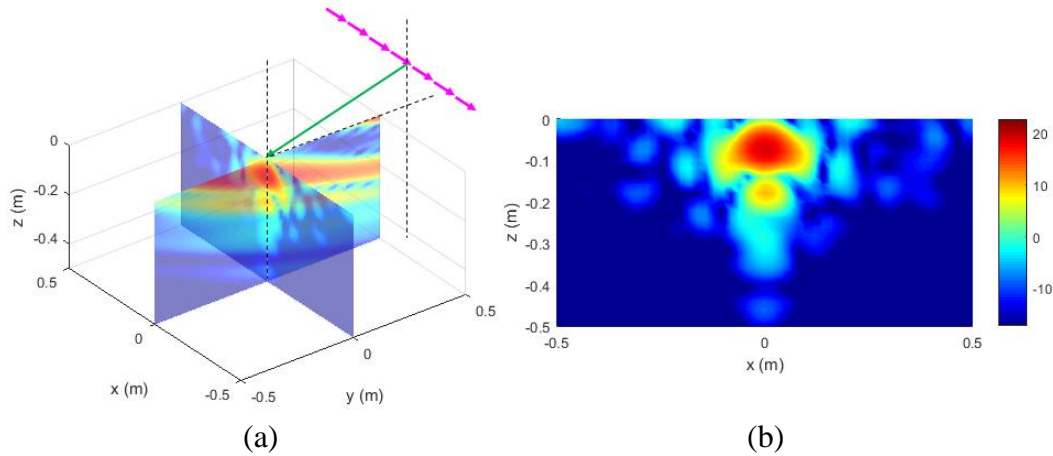


Fig. 31 SAR image of the M15 landmine buried under a rough ground surface obtained with the GPR system in side-looking configuration and H-H polarization: a) x-z and y-z planes, perspective view; b) x-z plane

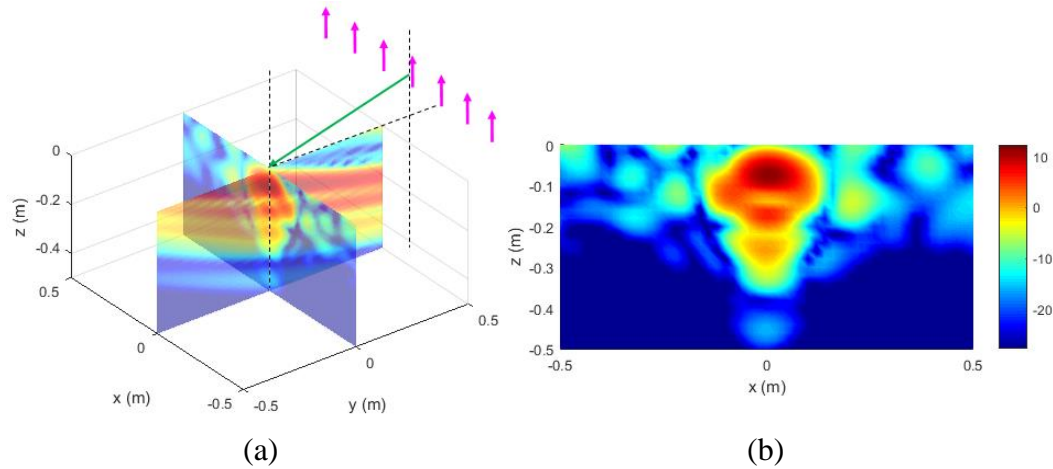


Fig. 32 SAR image of the M15 landmine buried under a rough ground surface obtained with the GPR system in side-looking configuration and V-V polarization: a) x-z and y-z planes, perspective view; b) x-z plane

5. PSF Analysis of a 3-D GPR SAR System

The SAR images in Sections 3 and 4 were created by modeling radar data collected along a linear aperture, which did not allow resolving the target in the y (or cross-track) direction. Nevertheless, it is of great interest to design a GPR imaging system that provides accurate target localization in all three dimensions. To achieve this, we have two possible solutions: 1) collect radar data over an aperture covering a 2-D area over the image volume and combine these data in a coherent 3-D image formation algorithm; or 2) collect independent radar data on different platforms, form separate SAR images based on these data, and combine them noncoherently to resolve the target in 3-D. The first solution involving coherent processing is

described in Section 5.1, while the second one, involving noncoherent processing, is described in Section 5.2.

5.1 Coherent GPR SAR System Using a 2-D Synthetic Aperture

If the synthetic aperture of the GPR system extends in both x and y directions, then we can use coherent SAR processing of all radar samples to obtain a 3-D image with resolution in all directions. In this section, we discuss only three configurations that allow this type of imaging: a rectangular 2-D array of uniformly spaced samples, a linear aperture describing a zigzag pattern and a circular aperture. Other aperture geometries for 3-D imaging can also be conceived; however, we think the three considered here are representative for this analysis and have reasonable chances to be implemented in practice.

The first type of synthetic aperture could be obtained by mounting a linear antenna array on the sUAV platform and moving it along a linear track in a direction orthogonal to the array. A schematic representation of the aperture samples characterizing this system is shown in Fig. 33, where we considered both the down-looking configuration (where the aperture is placed directly above the imaged volume, Fig. 33b) and the side-looking configuration (where the aperture is offset in the y direction with respect to the imaged volume, Fig. 33c). For the subsequent PSF simulations, we used the following aperture dimensions: 5 m in the x direction and 2 m in the y direction, with regular 10 cm spacing between samples in both directions. The other radar and target parameters are identical to those in Section 3.1. The radar is assumed to work in monostatic configuration, with each sample position designating a pair of Tx-Rx locations.

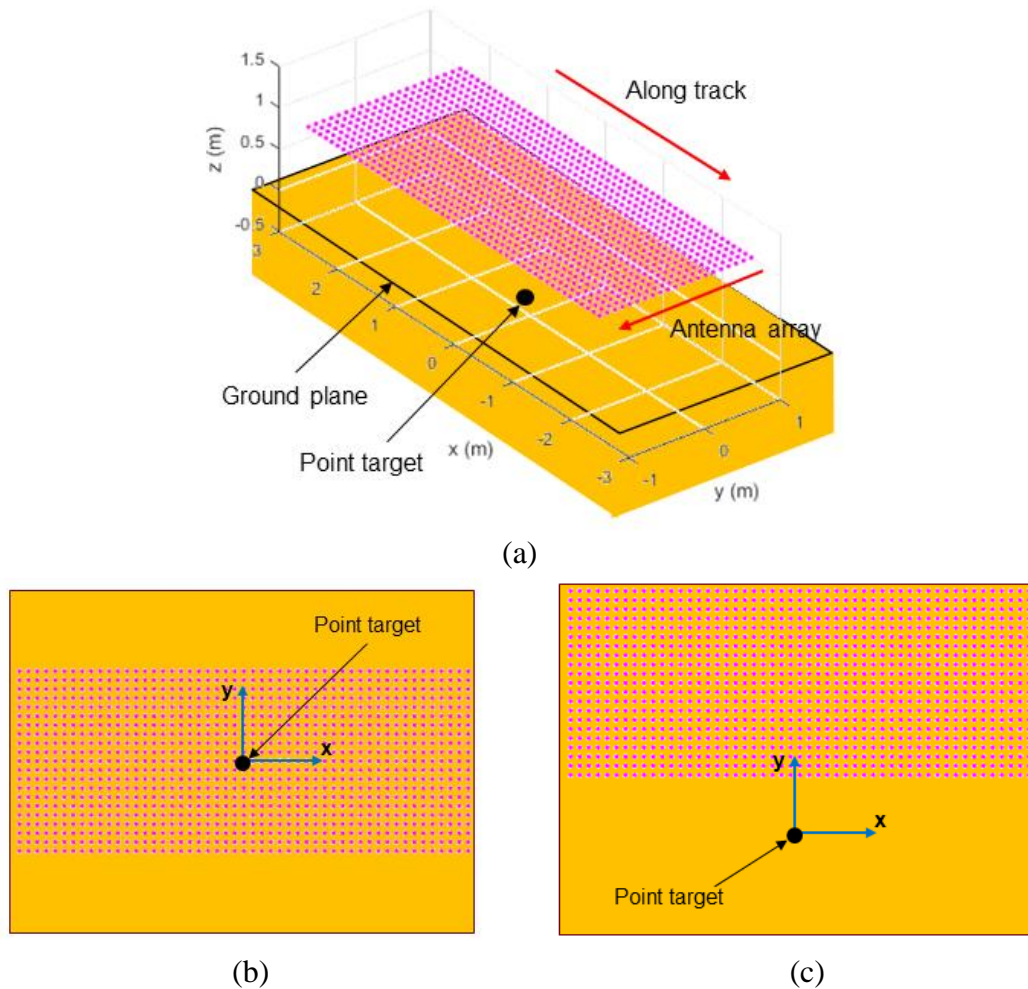


Fig. 33 Schematic representation of the GPR SAR system using a 2-D aperture for the formation of 3-D images: a) down-looking configuration, perspective view; b) down-looking configuration, top view; c) side-looking configuration, top view. The pink dots represent the aperture sample positions.

An important question is the practical feasibility of such a GPR system. While some current vehicle-mounted designs employ an antenna array in forward motion to generate 3-D images of the underground volume,¹⁴ installing a large array on an sUAV platform is more problematic. At issue are both the length and the weight of the array, but also the complexity of the wiring and electronics associated with a large number of elements. It is fair to say that the parameters considered in this study (2-m array length and 21 Tx-Rx pairs) are very optimistic, and a practical system would probably have to work with a smaller number of elements installed on a shorter mount. An additional comment is that the monostatic configuration does not necessarily achieve the best performance for the antenna array. Instead, a bistatic system using a full array of Rx's and only two Tx's at its ends^{6,7} yields better performance characteristics with a smaller number of elements. However, the

simulations presented here are primarily concerned with theoretical performance rather than feasibility issues.

Similarly to the analysis in Section 3.1 (Fig. 9), having a graphic representation of the radar signal amplitude across the aperture samples provides a good deal of information related to image resolution and sidelobes. For the rectangular 2-D aperture considered in this section, we obtain the amplitude maps in Fig. 34. As with the linear aperture, the H-H polarization in down-looking configuration displays a well-behaved amplitude variation, which yields the best resolution and smallest amount of sidelobes. The V-V polarization in down-looking configuration has a null in the middle of the aperture—this type of amplitude variation is expected to generate large sidelobes. The two side-looking cases display decreasing amplitudes as we increase the offset in the y direction, which is shown to have negative impact on the resolution and sidelobes in this direction.

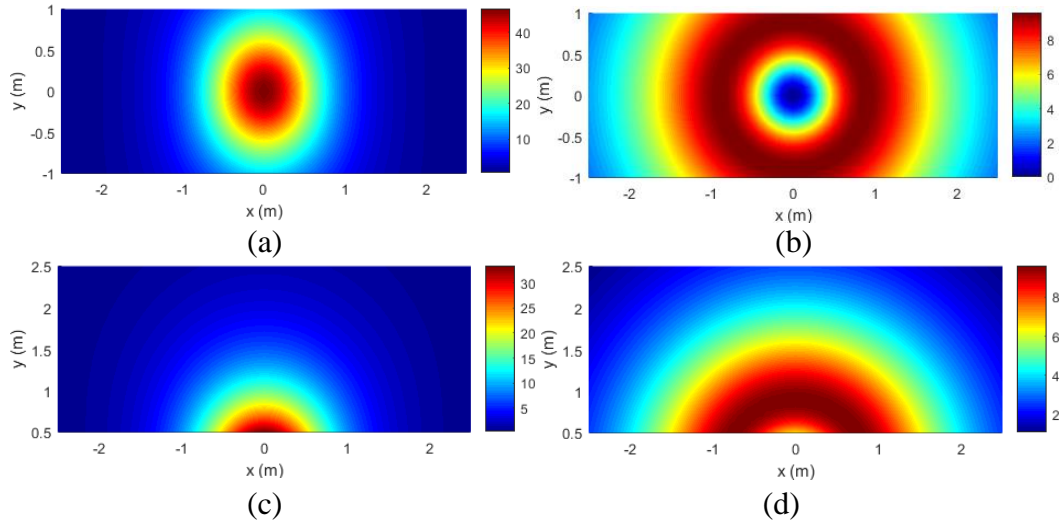


Fig. 34 Aperture amplitude weighting functions for the 2-D synthetic aperture considered in this section for: a) down-looking configuration, H-H polarization; b) down-looking configuration, V-V polarization; c) side-looking configuration, H-H polarization; d) side-looking configuration, V-V polarization. The 2-D maps are plotted in linear amplitude scale at a frequency of 1.25 GHz.

The results of the PSF simulations for the down-looking geometry are shown in Figs. 35 and 36, for H-H and V-V polarizations, respectively. As expected, the H-H images display a strong ground bounce and very good resolutions in both x and y directions. Notice that a small amount of sidelobes show up in the y direction (Fig. 35c), due to the fact that the aperture is too short in that direction (Eq. 12 requires 2.2 m to reach the resolution limit). The V-V polarization images are characterized by a much weaker ground bounce, but large sidelobe levels. Interestingly, the sidelobes in the y direction are not as pronounced as those in the x direction. We again attribute this anomaly to cutting the aperture short in the y direction.

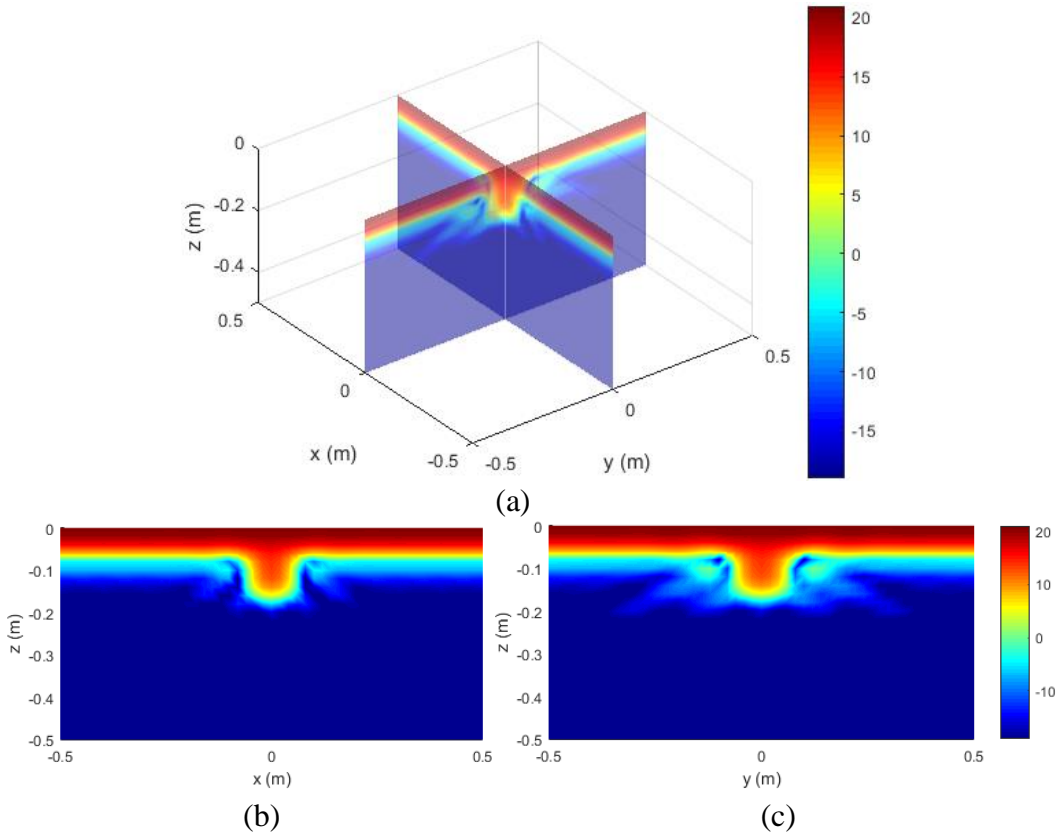


Fig. 35 Simulated PSF of a GPR system using a down-looking 2-D aperture and H-H polarization: a) x-z and y-z planes, perspective view; b) x-z plane; c) y-z plane

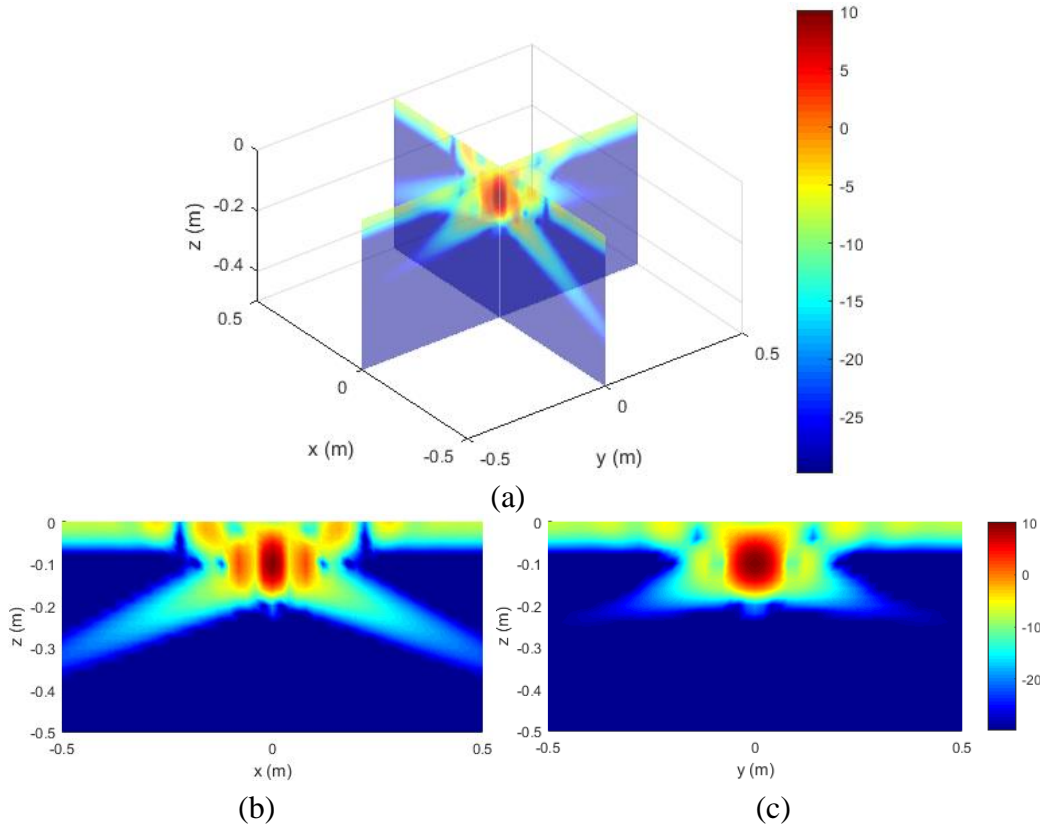


Fig. 36 Simulated PSF of a GPR system using a down-looking 2-D aperture and V-V polarization: a) x-z and y-z planes, perspective view; b) x-z plane; c) y-z plane

A more predictable result is obtained with a square 2-D aperture for the V-V polarization, as demonstrated in Fig. 37. In that simulation, the aperture length is 5 m in both directions. The image in Fig. 37d shows exactly the same sidelobe structure in the y - z plane as was previously obtained in the x - z plane. Needless to say, installing a 5-m-wide array with 51 elements on an sUAV platform does not seem a very reasonable proposition.

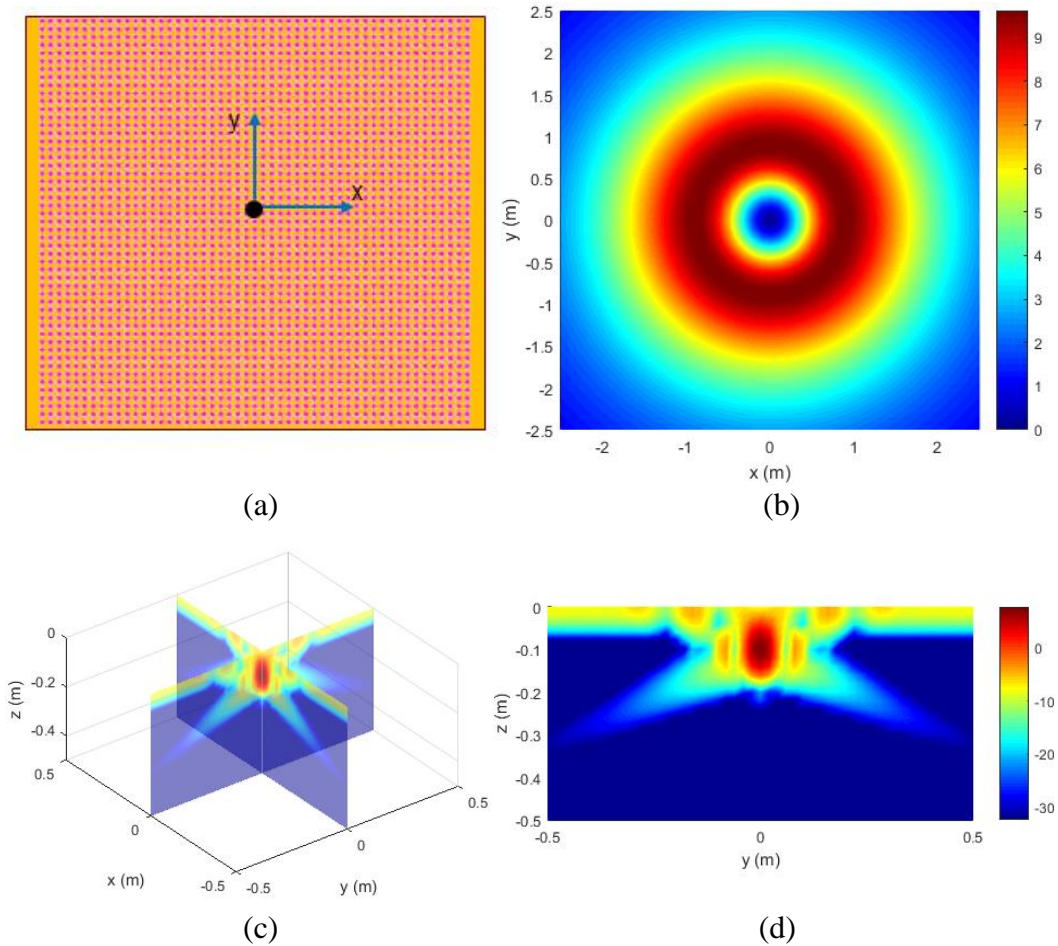


Fig. 37 Simulated PSF of a GPR system using a down-looking symmetric 2-D aperture and V-V polarization: a) schematic representation of the aperture samples; b) aperture amplitude weighting function at 1.25 GHz; c) x-z and y-z planes, perspective view; d) y-z plane

The images obtained in side-looking configuration are presented in Figs. 38 and 39 for the two polarization combinations. Although the ground bounce is reasonably separated from the target in these images, the resolution in the y direction is rather disappointing. For this reason, we do not see the 2-D aperture in side-looking configuration as a good solution to operate a GPR system for 3-D imaging of underground targets.

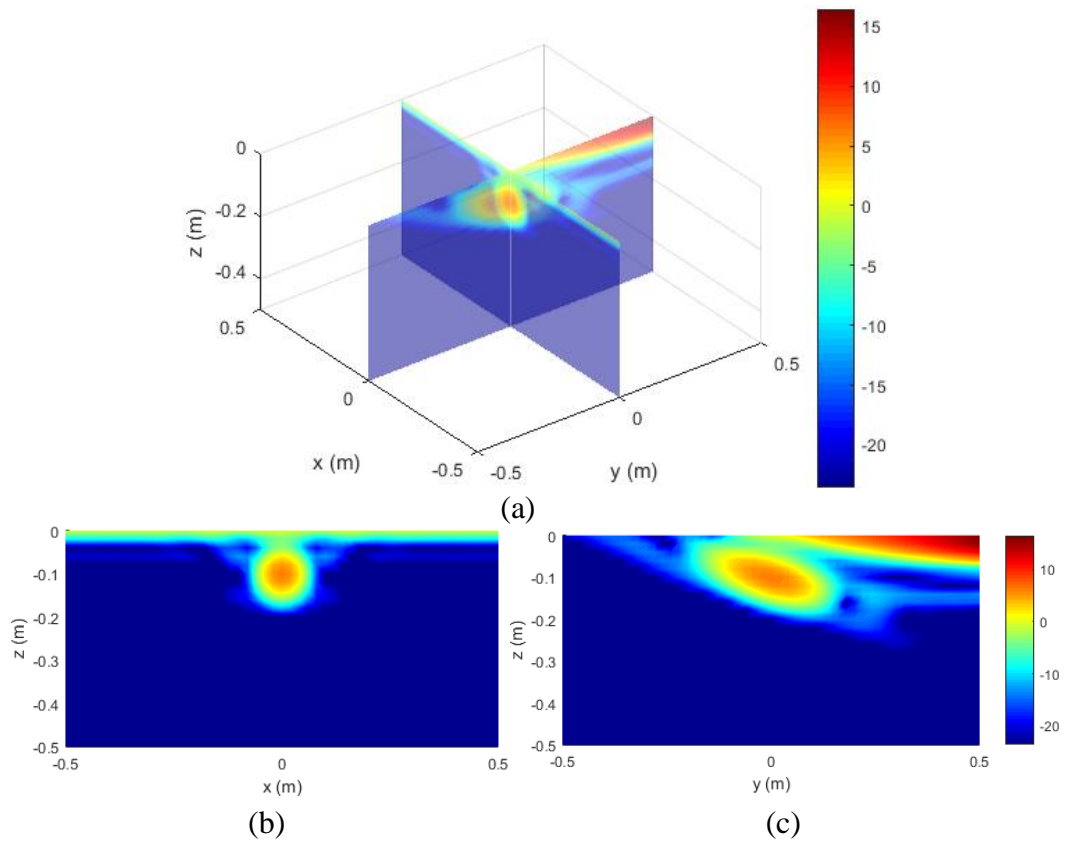


Fig. 38 Simulated PSF of a GPR system using a side-looking 2-D aperture and H-H polarization: a) x-z and y-z planes, perspective view; b) x-z plane; c) y-z plane

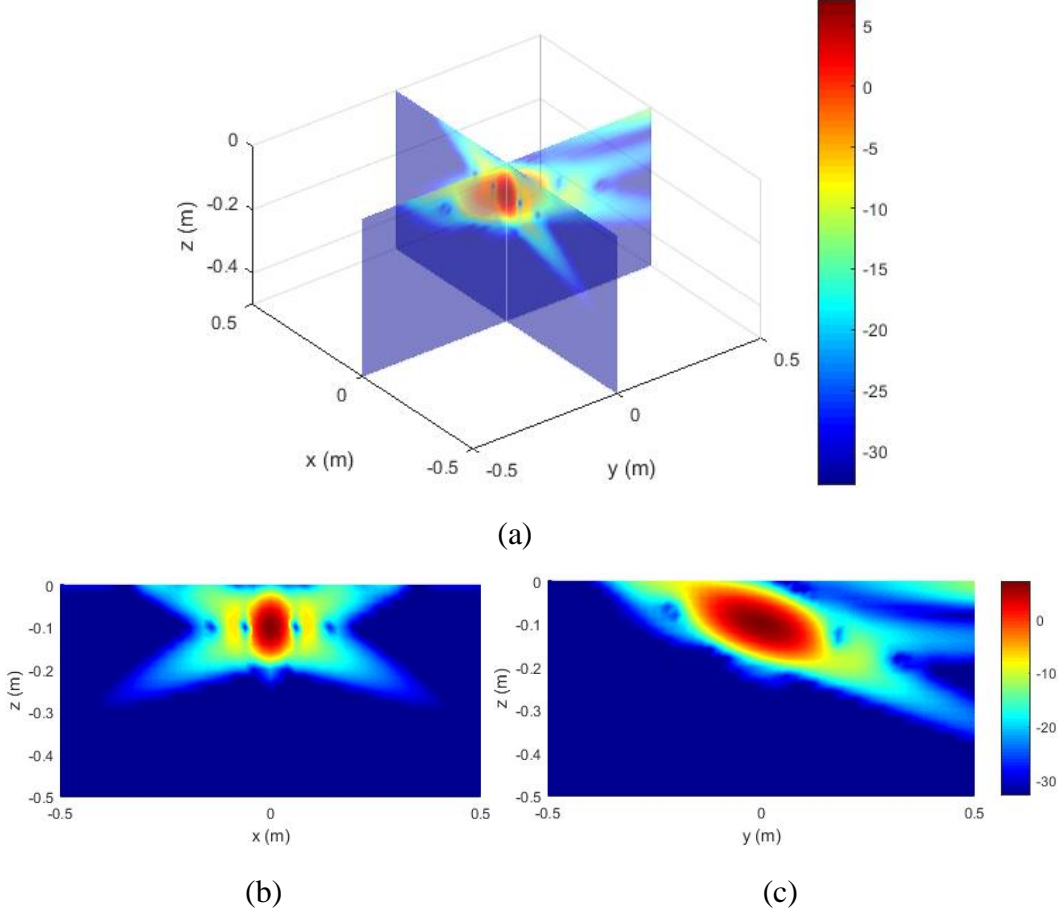


Fig. 39 Simulated PSF of a GPR system using a side-looking 2-D aperture and V-V polarization: a) x-z and y-z planes, perspective view; b) x-z plane; c) y-z plane

To explain the loss of resolution in y direction as we transition from down-looking to side-looking geometry, we need to establish the equations characterizing this resolution. First, for a down-looking aperture covering the entire image footprint, the y -directed resolution is computed the same as the x -directed resolution (see Eq. 9), assuming the antenna array is long enough to reach the $\frac{\lambda_0}{4}$ resolution limit. For a side-looking aperture with an average lateral offset $Y_{off} = \frac{Y_{offa} + Y_{offb}}{2}$ we obtain the following formula for the y -directed resolution:

$$\delta y = \frac{\lambda_0}{2\sqrt{\epsilon_r}(\sin \theta_{gb} - \sin \theta_{ga})\cos \theta_{sg}} = \frac{\lambda_0}{2(\sin \theta_b - \sin \theta_a)\cos \theta_{sg}}, \quad (19)$$

where $\cos \theta_{sg} = \cos \frac{\theta_{ga} + \theta_{gb}}{2} = \sqrt{1 - \frac{Y_{off}^2}{\sqrt{\epsilon_r}(Y_{off}^2 + h^2)}}$ (see Fig. 40). Although the θ_{sg} angle is typically small so $\cos \theta_{sg} \cong 1$ (as in the x - z plane propagation analysis in

Section 3.2), the factor $\sin \theta_b - \sin \theta_a$ in the denominator is the main cause for the increase in δy for this scenario. The amplitude variation across aperture in the y direction (see Figs. 34c and 34d) also contributes to the poor resolution, in addition to the elevated sidelobe levels. In conclusion, the loss of lateral resolution in side-looking configuration can be explained by the squinted geometry of the aperture in the y direction with respect to the image domain.

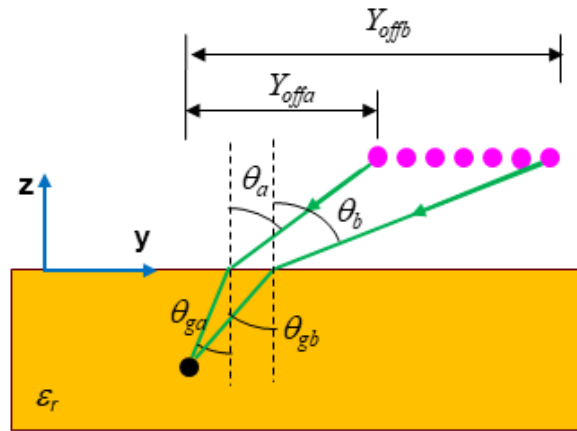


Fig. 40 Geometry of the side-looking GPR SAR system for 3-D imaging showing the parameters relevant to the y -direction resolution calculations

An alternative synthetic aperture geometry that covers a 2-D area and thus enables the formation of 3-D images is described in Fig. 41, where the radar system is equipped with only one Tx-Rx pair of elements and the platform moves along a zigzag pattern. The main advantage of this configuration is the simplicity of the system (similar to that considered in Sections 3 and 4), which now avoids the need for a complex antenna array. One obvious downside though is the slower area coverage as compared to the configuration described in Fig. 33. The synthetic aperture in Fig. 41 covers the same overall area as the 2-D aperture in Fig. 33: 5 m in the x direction and 2 m in the y direction, with a linear spacing of 4.2 cm between samples, measured along each arm of the zigzag pattern. The total number of aperture samples employed in the image formation is 400.

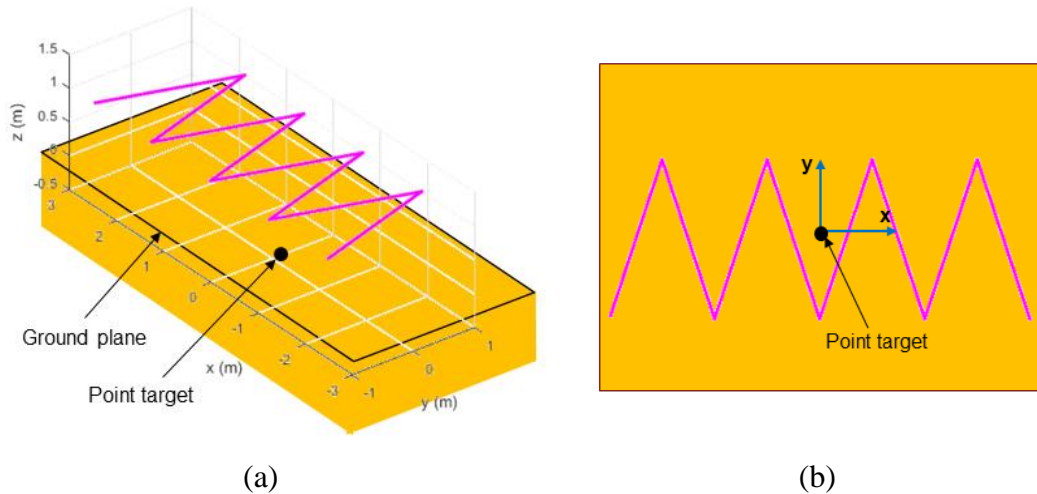


Fig. 41 Schematic representation of the GPR SAR system using a zigzag-type of aperture for the formation of 3-D images: a) perspective view; b) top view. The pink dots represent the aperture sample positions.

Examples of the images that can be obtained with such a system are presented in Figs. 42 and 43, for H-H and V-V polarization, respectively. These images resemble those in Figs. 35 and 36, obtained with the rectangular 2-D aperture. However, due to the sparse nature and irregular spacing of the aperture samples in both x and y directions for the zigzag pattern, the images in Figs. 42 and 43 display stronger artifacts caused by a combination of sidelobes and grating lobes. It is also apparent that the target-to-ground-bounce ratio is weaker in these images than in those from Figs. 35 and 36. Simulations were also run with a zigzag-pattern aperture in side-looking configuration. Predictably, the resulting images were afflicted by the same problems as in the down-looking case, in addition to the relatively poor resolution in the y direction.

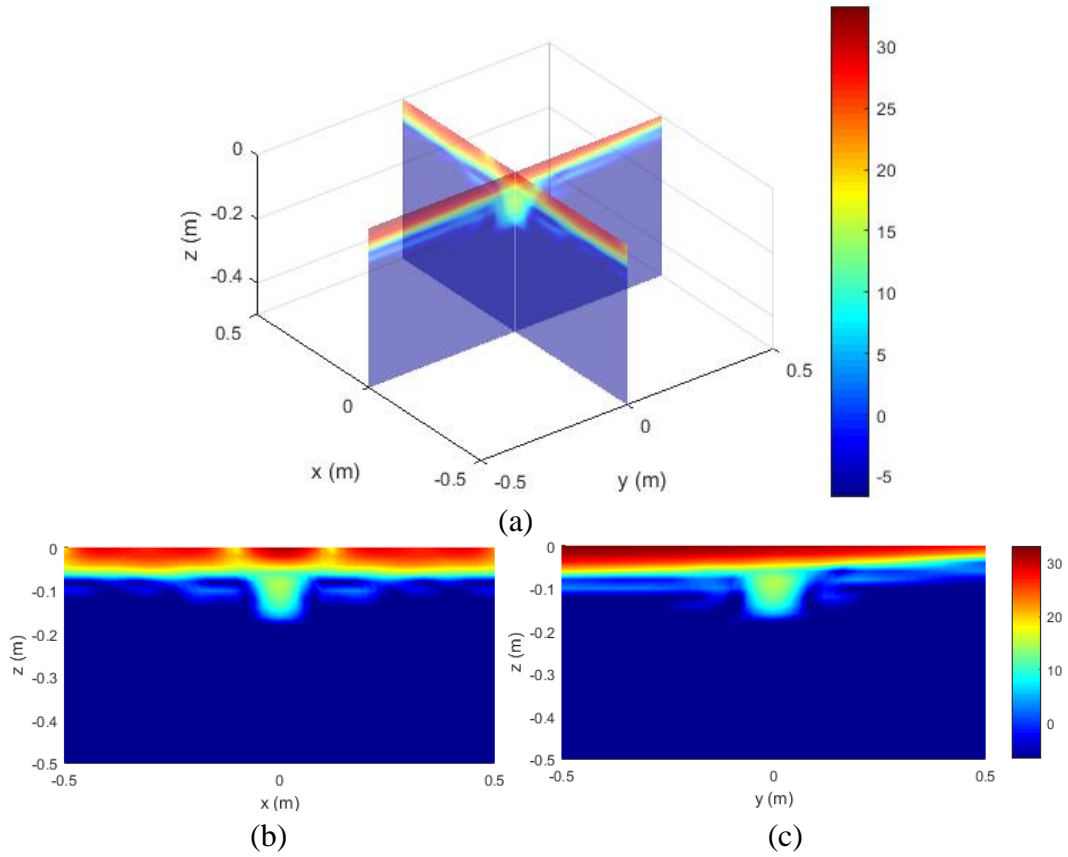


Fig. 42 Simulated PSF of a GPR system using a zig-zag aperture as described in Fig. 36 and H-H polarization: a) x-z and y-z planes, perspective view; b) x-z plane; c) y-z plane

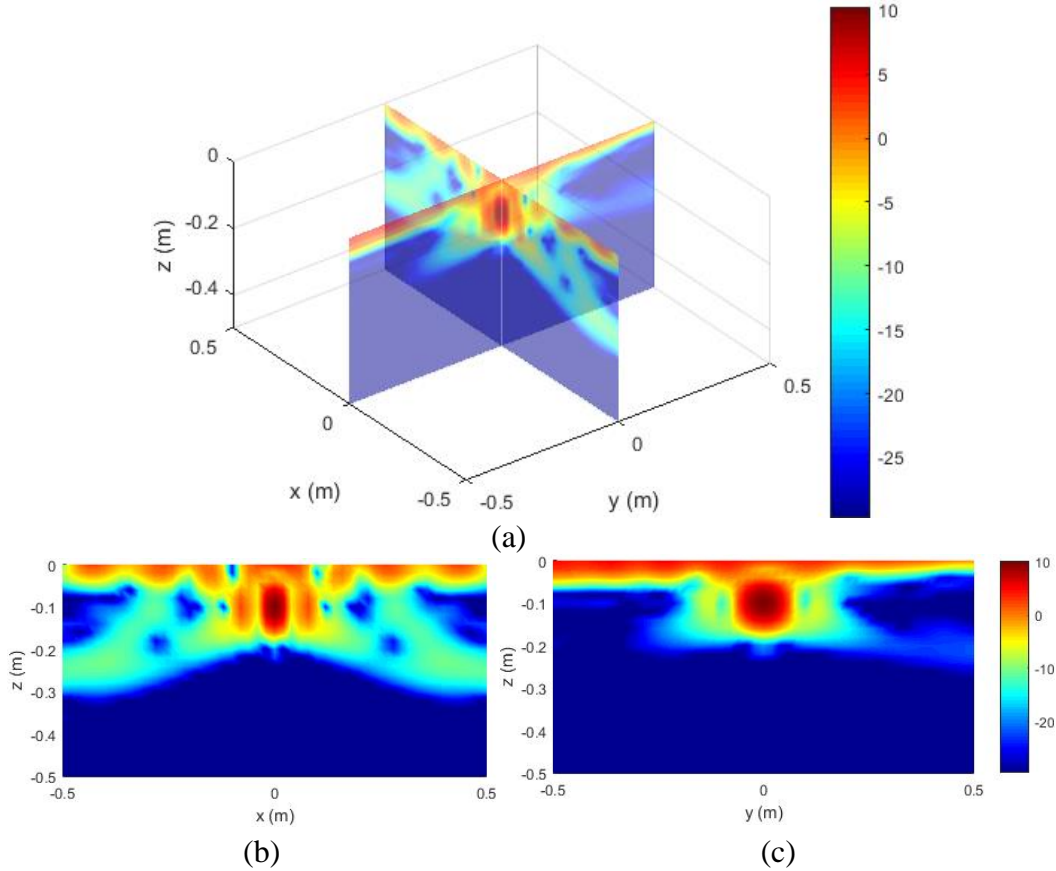


Fig. 43 Simulated PSF of a GPR system using a zig-zag aperture as described in Fig. 36 and V-V polarization: a) x-z and y-z planes, perspective view; b) x-z plane; c) y-z plane

A third type of synthetic aperture geometry allowing the formation of 3-D images describes a circle in a horizontal plane around the target location (Fig. 44). An analysis of this 3-D SAR configuration can be found in Soumekh.¹⁵ The primary issue with this sensing modality is the requirement of knowing the general target location a priori. One possible way to operate a GPR SAR system on an sUAV is to perform a 2-D scan of a stretch of terrain in strip-map mode, using a linear synthetic aperture, find areas of interest that can potentially feature a target (even though the image may be imperfect), then return and circle around these areas to form high-resolution, 3-D images of those volumes in spotlight SAR mode. These images may contain enough details to allow discrimination of the targets of interest from clutter objects, and possibly automatic target recognition.

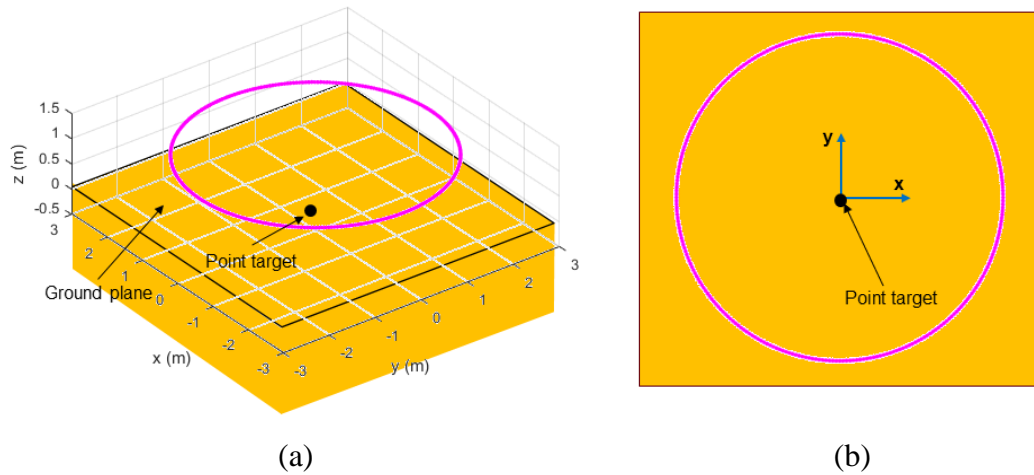


Fig. 44 Schematic representation of the GPR SAR system using a circular aperture for the formation of 3-D images: a) perspective view; b) top view. The pink dots represent the aperture sample positions

Images obtained by this SAR geometry are shown in Figs. 45 and 46, for H-H and V-V polarizations, respectively. The circle has a radius of 2.5 m, at a height of 1 m and there are 300 aperture samples within a full rotation. Notice that there are no major differences between the two polarization combinations in this case. For the H-H polarization, the dipole antenna orientation changes at each aperture sample, such that the dipole moment vector is always perpendicular to the LOS pointing to the middle of the image volume (this is consistent with the way a spotlight SAR system operates).⁹ If the target is not placed in the middle of the circle, its image will present some asymmetries. Other features to notice in these images are the excellent resolution in the x and y directions (its analysis¹⁵ differs from that presented in Section 3.2), as well as the large sidelobes levels.

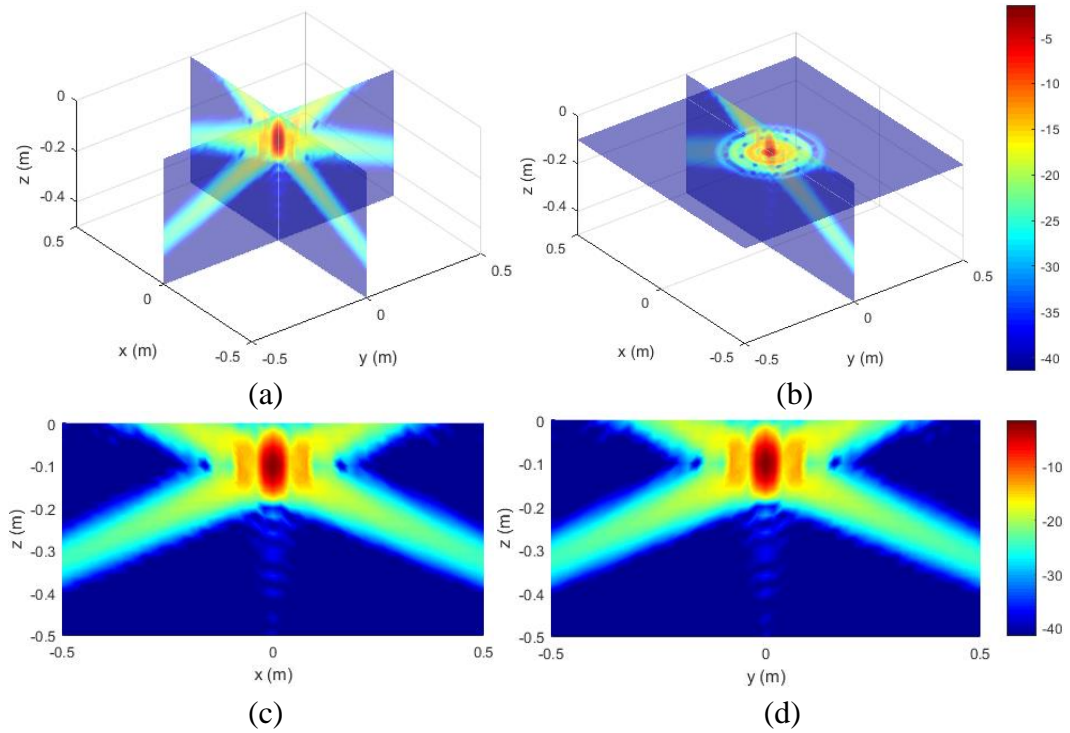


Fig. 45 Simulated PSF of a GPR system using a circular aperture as described in Fig. 44 and H-H polarization: a) x-z and y-z planes, perspective view; b) x-z and x-y planes, perspective view; c) x-z plane; d) y-z plane

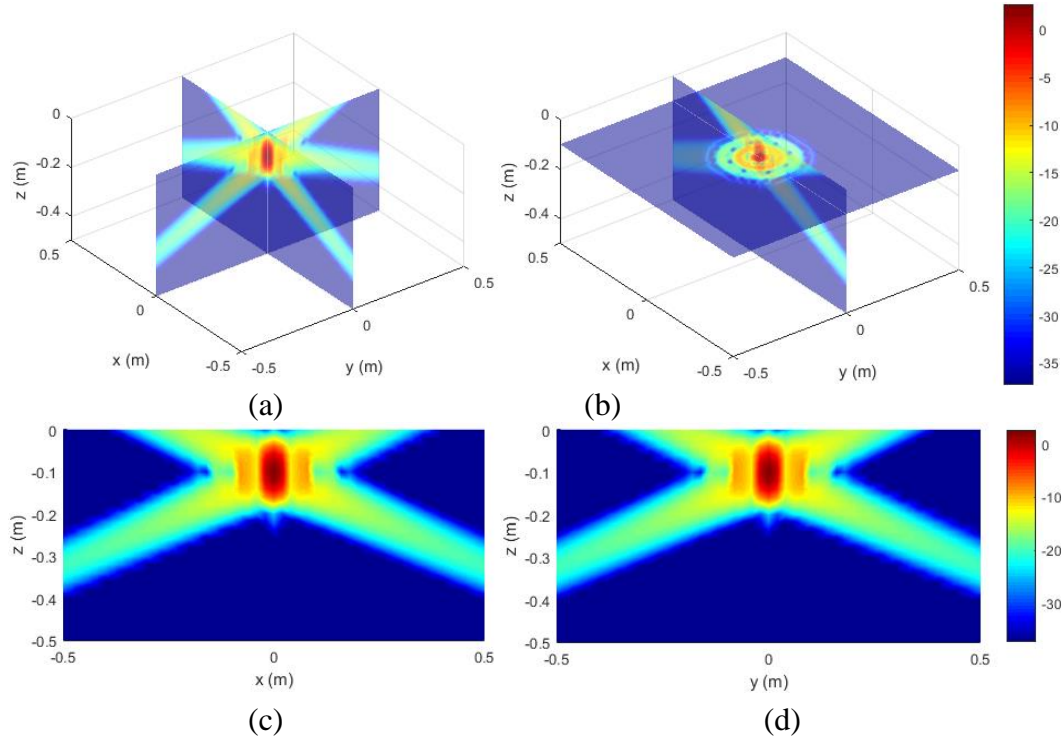


Fig. 46 Simulated PSF of a GPR system using a circular aperture as described in Fig. 44 and V-V polarization: a) x-z and y-z planes, perspective view; b) x-z and x-y planes, perspective view; c) x-z plane; d) y-z plane

5.2 Noncoherent GPR Imaging Using Multiple SAR Systems

The 3-D imaging options examined in Section 5.1 have some obvious drawbacks. For down-looking configurations, the H-H polarization has the issue of the strong ground bounce, while the V-V polarization displays large sidelobes (same as the 2-D imaging systems). The side-looking configurations solve both these issues, but achieve poor resolution in the y direction, due to the aperture squint with respect to the image volume. Another problem with the rectangular 2-D aperture is the need for an antenna array, which makes the system heavier and more complex/expensive. Attempts to mitigate this problem by using a zigzag or circular trajectory and a single Tx-Rx channel pair come with their own drawbacks.

A completely different approach to 3-D GPR imaging is to noncoherently combine images obtained by independent systems employing linear synthetic apertures. These systems can be equipped with single Tx-Rx channel pairs and operate the same as the SAR systems modeled in Sections 3 and 4.

An example of this type of data collection and processing is shown in Figs. 47 and 48. This concept involves two linear-track SAR systems operating in side-looking configuration, with a symmetric geometry with respect to the point target, as in

Fig. 47. The two images obtained by those systems in the y - z plane are shown in the upper part of Fig. 48, where we labeled the two as “left” and “right”. As expected, these individual images cannot resolve the target in the y direction and we obtain the two oblique streaks characteristic to this imaging geometry. However, if we combine the two images using the following voxel-wise operation:

$$I(\mathbf{r}) = \arg \min \left\{ |I_{left}(\mathbf{r})|, |I_{right}(\mathbf{r})| \right\}, \quad (20)$$

we can isolate the diamond-shape feature at the intersection of the two streaks around the target location. Note that in Eq. 20 the \arg symbol refers to the modulus (or absolute value) operator, meaning we pick the complex value of the voxel with minimum magnitude between the two choices.

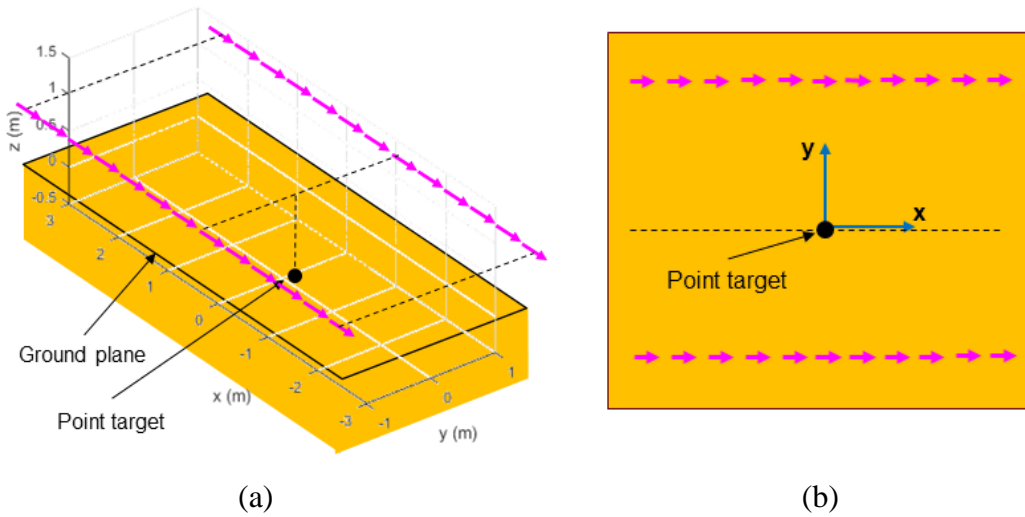


Fig. 47 Schematic representation of the GPR SAR system using two linear apertures for the noncoherent formation of 3-D images: a) perspective view; b) top view

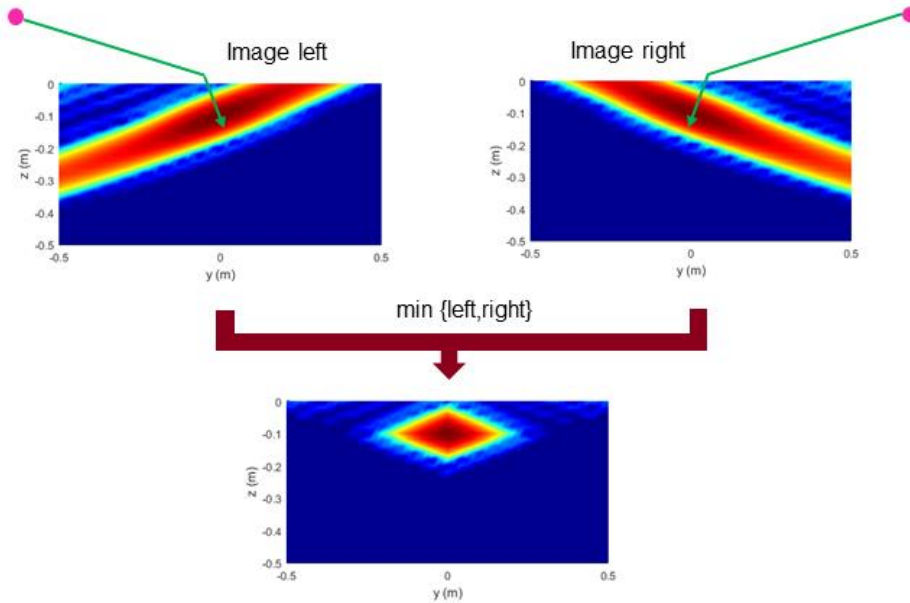


Fig. 48 Illustration of the principle underlying the noncoherent SAR image combination, which allows one to resolve the target in the y direction

The complete PSF simulation results using this approach are shown in Figs. 49 and 50, for H-H and V-V polarizations, respectively. In these simulations, we used side-looking synthetic apertures with lateral offsets of 1.5 m on each side of the target location, with all the other radar parameters identical to those in Section 3. These images achieve resolution in all three dimensions and avoid the ground bounce, thanks to the side-looking geometry on which the original images are based. Additionally, this type of imaging system should be relatively easy to implement in practice, since the two radar sensors can operate independently. In fact, one can use a single GPR system and two successive passes on different tracks to obtain the same images. The only additional requirement is that the two original SAR images be registered on the Earth coordinate grid with sufficient accuracy (typically on the order of a resolution cell size).

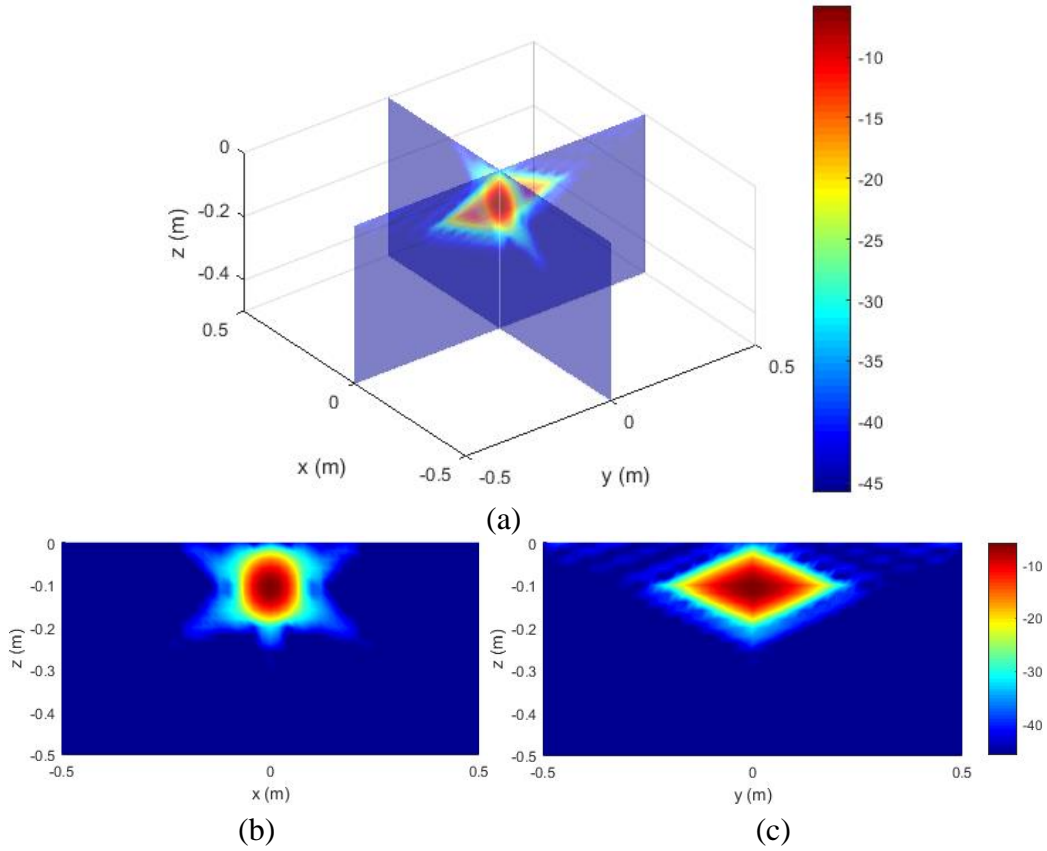


Fig. 49 Simulated PSF obtained through the noncoherent combination of the images created by two linear-aperture SAR systems described in Fig. 47, in H-H polarization: a) x-z and y-z planes, perspective view; b) x-z plane; c) y-z plane

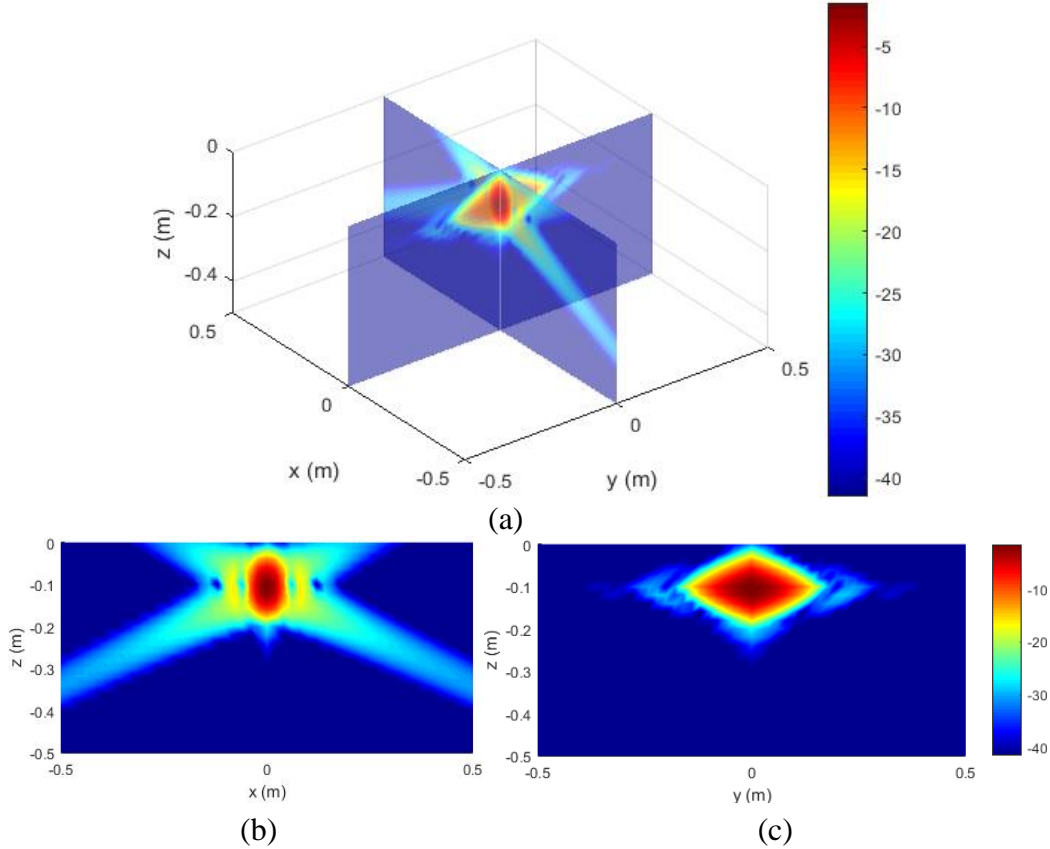


Fig. 50 Simulated PSF obtained through the noncoherent combination of the images created by the linear-aperture SAR systems described in Fig. 47: a) x-z and y-z planes, perspective view; b) x-z plane; c) y-z plane

When the two side-looking synthetic apertures are not perfectly symmetric with respect to the target location, the shape of the resulting image in the y-z plane may change slightly, although the resolution should be similar to that obtained in Figs. 49c and 50c. The extensive discussion in Section 3.2 related to the radar wave propagation inside the ground should make it clear by now that the orientation angles of the two streaks visible in Fig. 48 (upper part) do not change much with the aperture offsets with respect to the target location.

We also performed simulations using three different linear SAR tracks, two in side-looking and one in down-looking configurations, and combined the three separate images by the noncoherent operation in Eq. 20. The resulting image (not shown here) does not demonstrate any enhancement as compared to those in Figs. 49 and 50.

Although they allow resolving the target in the cross-track direction, the images in the y-z plane obtained by the noncoherent procedure previously described (Figs. 49c and 50c) do not display the same well-focused PSFs as the 3-D images presented in Section 5.1. The main issue with this particular procedure is the large

overlap between the two images obtained from linear apertures placed on either side of the target. Ideally, we would like the two oblique streaks in the upper part of Fig. 48 to be orthogonal to one another, with minimal overlap between the two. However, this situation is physically impossible to achieve because the wave propagation angle inside the ground is limited by the critical angle, which forces the two streaks to lie at an angle close to horizontal.

A better configuration for noncoherent processing of GPR images is shown in Fig. 51, where the two linear apertures are orthogonal to one another (one along the x axis and the other along the y axis). The PSF images created by each aperture now display elongated streaks stretching in orthogonal planes (y - z and x - z , respectively). Combining them via the procedure described by Eq. 20 leads to well-focused 3-D images of the target, as shown in Figs. 52 and 53. To create these images, we used the same parameters as in the previous numerical example, with aperture lengths of 10 m and lateral offsets of 1.5 m for both aperture orientations.

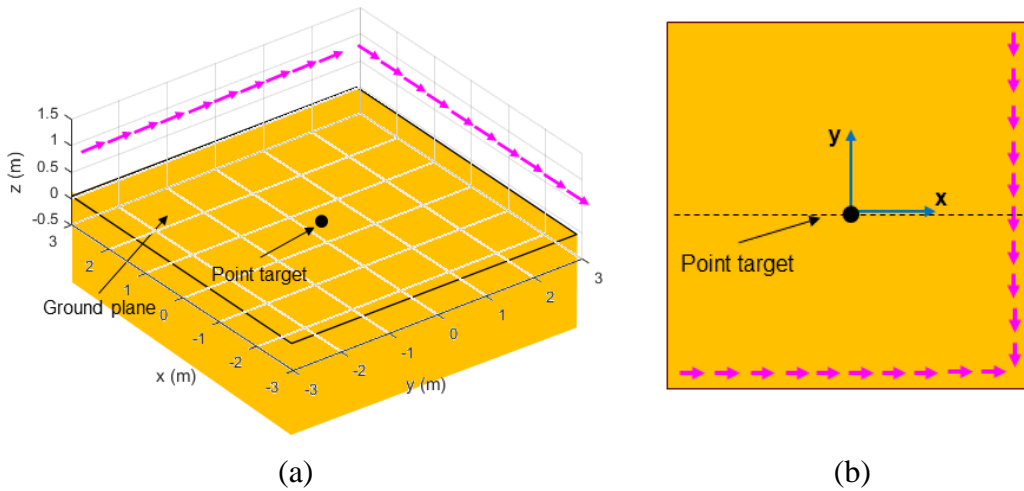


Fig. 51 Schematic representation of the GPR SAR system using two orthogonal linear apertures for the noncoherent formation of 3-D images: a) perspective view; b) top view

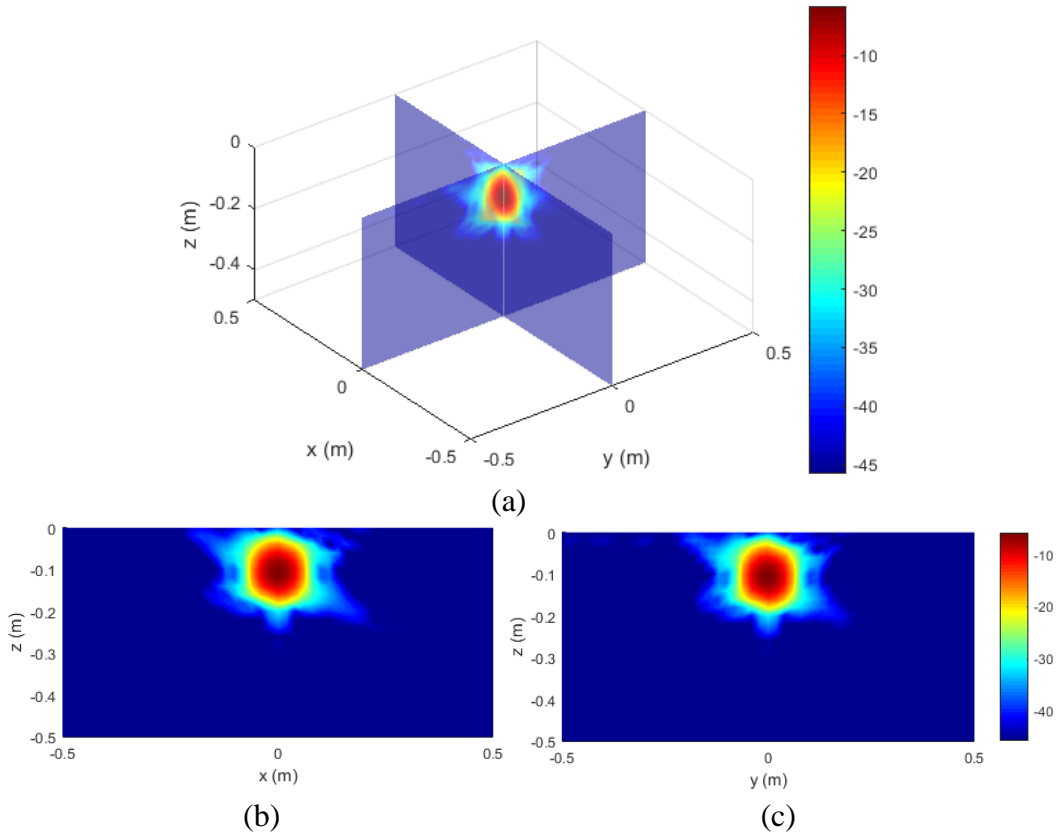


Fig. 52 Simulated PSF obtained through the noncoherent combination of the images created by two SAR systems with orthogonal apertures described in Fig. 51, in H-H polarization: a) x-z and y-z planes, perspective view; b) x-z plane; c) y-z plane

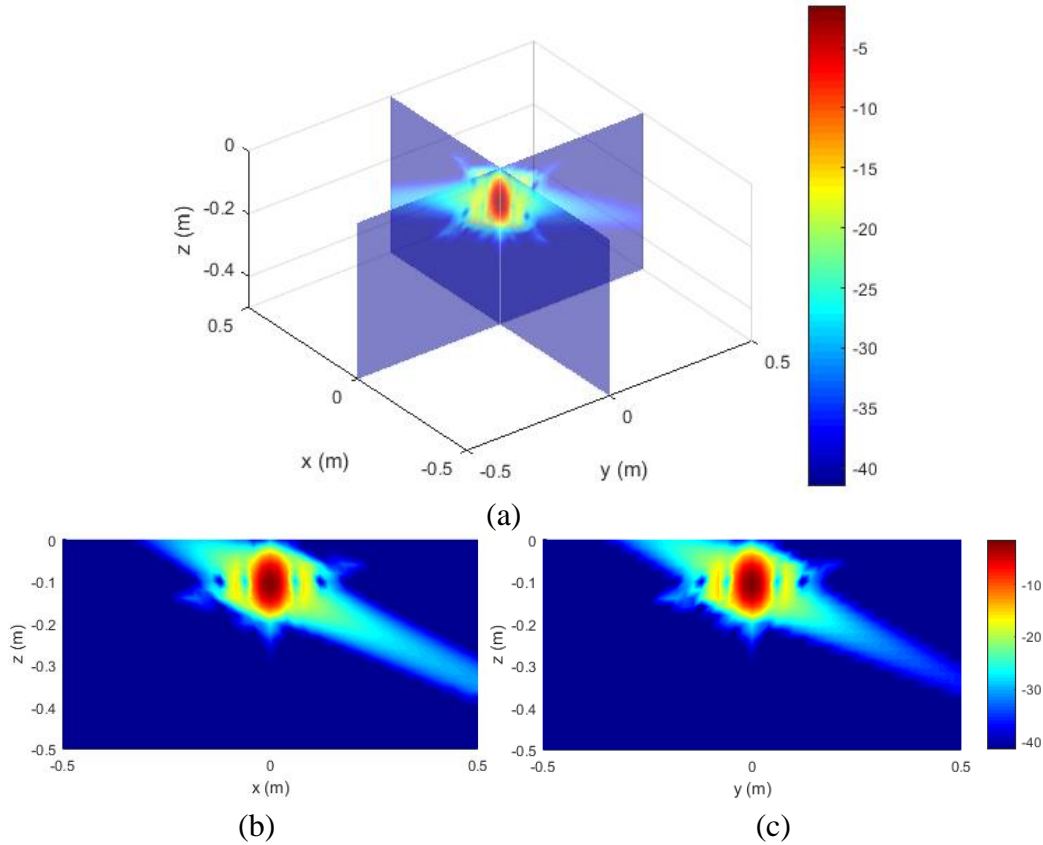


Fig. 53 Simulated PSF obtained through the noncoherent combination of the images created by two SAR systems with orthogonal apertures described in Fig. 51, in V-V polarization: a) x-z and y-z planes, perspective view; b) x-z plane; c) y-z plane

As with the circular aperture configuration in Section 5.1, realizing the sensing geometry described in Fig. 51 is far from straightforward from an operational standpoint, since a priori information on the target location is needed to perform radar scanning of the area along two mutually orthogonal directions. Again, collecting radar data in this configuration should be preceded by a simple linear scan along one direction. The 2-D images generated by these data would be able to indicate a number of areas of interest where the platform could return to perform an additional scan along the perpendicular axis. The high mobility, precise control, and possible task autonomy of modern sUAVs make these devices very attractive platforms for operating an imaging radar in one of the modalities discussed in this report. Undoubtedly, future research will reveal different aperture geometries and processing schemes for increased imaging performance.

6. Conclusions

In the concluding section of this report, we review the steps performed during this investigation and present a summary of the findings. In Part I of this study¹ we discussed the current status of the GPR technology and explained how the newly proposed GPR system mounted on an sUAV can solve multiple outstanding issues with the current technology.

A large portion of the investigation was dedicated to analyzing the imaging performance of the proposed GPR system. The main tool employed in this analysis was the PSF, which represents the image obtained in the presence of a point target. The theoretical development of the radar wave propagation for GPR systems (presented in Part I of the study) allowed us to formulate the imaging algorithm based on the matched filter method, as well as the equations needed for PSF calculations.

The PSF was first investigated for 2-D GPR imaging systems, using a linear synthetic aperture. Image metrics such as resolution, grating lobes, and sidelobes were analyzed both theoretically and by numerical examples. We compared the performance of systems operating in down- and side-looking configurations, as well as in H-H and V-V polarizations. We found some important differences between these modalities due to variations in the received signal magnitude across the synthetic aperture. Other metrics such as signal power and sensitivity to positioning errors were also discussed in Section 3.

Some of the simulation scenarios used for PSF calculations were repeated with radar scattering data generated by the AFDTD modeling software. The target was a metallic antitank landmine (M15), typical for CEH applications. Since the scattering phenomenology of this target is much more complex than that of a point target, a high-resolution imaging system may be able to separate certain features to be used by a target identification algorithm.

We also proposed several synthetic aperture geometries that would allow the formation of 3-D images of the underground volume. These include 2-D arrays of spatial samples, a linear aperture describing a zigzag pattern over the image domain, and a circular aperture over the same domain. Yet another possibility presented here is to noncoherently combine the images obtained by two or more linear apertures in side-looking configurations. While this study did not discuss the feasibility of these sensor systems, it is clear that solutions involving only one Tx-Rx channel pair per system and avoiding complex synchronization schemes between separate platforms have better chances to succeed in practice.

A summary of this report's findings with implications to the GPR system design is presented here in bullet format as follows:

- The down-looking configuration combined with H-H polarization offers the best performance metrics. This is consistent with the fact that most current GPR systems employ these modalities. Their only drawback is the strong ground bounce present in the SAR image, which may reduce the chances of detection for shallow buried targets. For deep buried targets, this configuration clearly provides the best detection performance.
- For 2-D imaging of buried targets, the side-looking configuration is a good alternative to the traditional down-looking GPR system, offering the advantage of good separation between the ground bounce and the target in the SAR image. Either H-H or V-V polarization can be used for this configuration, with no clear winner between the two.
- An UWB GPR SAR system can provide down to 10 cm of image resolution in depth and cross-range directions, which is typically adequate for resolving most targets of interest.
- Sidelobes and grating lobes are automatically attenuated by the GPR imaging system. The sidelobe suppression is due to the natural tapering down of the signal scattered by the target as the radar moves away from it along the aperture. The grating lobe attenuation is mainly caused by the UWB nature of the radar waveforms.
- The image resolution has very weak dependence on the radar platform height and lateral aperture offset, as well as the target depth. Much of this effect has to do with the radar wave refraction at the air-ground interface, which typically dictates a steep propagation angle inside the ground. However, to achieve the theoretical cross-range resolution limit, a minimum integration length along the synthetic aperture is required, which increases with both the height and the lateral offset. This integration length is relatively short, only a few meters when the platform height is about 1 m.
- The penalty in terms of depth and cross-range resolutions for choosing the side-looking over the down-looking sensing geometry is quite small, of maximum 12% for the simulation scenarios in this report. However, there is a significant loss of signal power (of about 10 dB) in side-looking configuration as compared with the down-looking counterpart in H-H polarization.
- The GPR system should operate in a frequency band between 0.5 and 2.5 GHz, which is consistent with most current designs.

- The GPR SAR system is fairly tolerant to platform positioning errors. Our simulations suggest a maximum RMS positioning error of 3 cm before the PSF peak degrades to unacceptable levels. This kind of positioning accuracy should be readily achievable with current GPS technology.
- For slightly rough ground, the surface clutter has very limited impact on the side-looking images, as well as on the down-looking, H-H polarization images.
- For coherent 3-D GPR imaging systems, the side-looking aperture geometry provides poor resolution in the cross-track (lateral) direction, due to the squinted sensing geometry. One good solution in terms of resolution in all directions consists of using a down-looking 2-D aperture and H-H polarization. However, this modality presents again the issue of strong ground bounce interfering with target detection. Alternatively, a circular aperture offers very good resolution in all directions, but large sidelobe levels.
- The noncoherent combination of images obtained by two or more linear synthetic aperture systems can provide resolution in all directions, while avoiding the ground bounce issue. Although a simple noncoherent processing algorithm was suggested in this report, additional research is needed to further develop this idea.

Multiple issues related to the principles, design, and operation of an sUAV-based GPR system remain to be investigated in future work. In terms of modeling, more realism can be introduced in the radar sensing scenarios by including soil inhomogeneities, as well as other types of targets. The choices of radar waveforms and hardware architecture are critical elements in the system design. Once these choices are made, we can perform more detailed calculations to determine other system parameters, such as timing and power. The integration of the radar system on an sUAV platform is another difficult task for the future sensor design. Finally, it is clear that the discussion of 3-D GPR imaging systems in Section 5 is incomplete, and new ideas may provide superior solutions with reasonable cost and complexity.

7. References

1. Dogaru T. Imaging study for small-UAV-mounted ground penetrating radar: part I – methodology and analytic formulation. Adelphi (MD): Army Combat Capabilities Development Command Army Research Laboratory (US); 2019 Mar. Report No.: ARL-TR-8654.
2. Balanis C. Advanced engineering electromagnetics. New York (NY): Wiley; 1989.
3. Richards M, Scheer J, Holm W. Principles of modern radar – basic principles. Raleigh (NC): SciTech Publishing; 2010.
4. Dogaru T. Doppler processing with ultra-wideband (UWB) radar revisited. Adelphi (MD): Army Research Laboratory (US); 2018 Jan. Report No.: ARL-TN-0866.
5. Kirose G, Sherbondy K, Smith G. Permittivity measurements of the soil at Yuma Proving Ground (YPG), Engineering Common Use Test Site (ECUTS) and Counter Mine Test Site (CMTS) to support the iRadar field experiment. Adelphi (MD): Army Research Laboratory (US); 2014 Mar. Report No.: ARL-TN-0595.
6. Ressler M, Nguyen L, Koenig F, Wong D, Smith G. The ARL synchronous impulse reconstruction (SIRE) forward-looking radar. Proc. SPIE. 2007;6561.
7. Phelan B, Ranney K, Gallagher K, Clark J, Sherbondy K, Narayanan R. Design of ultra-wideband (UWB) stepped-frequency radar (SFR) for imaging of obscured targets. IEEE Sensors Journal. 2017;17(14).
8. Dogaru T. Model-based radar power calculations for ultra-wideband (UWB) synthetic aperture radar (SAR). Adelphi (MD): Army Research Laboratory (US); 2013 Jun. Report No.: ARL-TN-0548.
9. Melvin W, Scheer J. Principles of modern radar – advanced techniques. Edison (NJ): SciTech Publishing; 2013.
10. Dogaru T. Synthetic aperture radar for helicopter landing in degraded visual environments. Adelphi (MD): Army Research Laboratory (US); 2018 Dec. Report No.: ARL-TR-8595.
11. NovAtel CORRECT with RTK. NovAtel Inc. [accessed 2019 June 25]. <https://www.novatel.com/products/correct-rtk>.

12. Dogaru T. NAFDTD – A near-field finite difference time domain solver. Adelphi (MD): Army Research Laboratory (US); 2012 Sep. Report No.: ARL-TR-6110.
13. Bryant R, Moran MS, Thoma DP, Holifield Collins CD, Skirvin S, Rahman M, Slocum K, Starks P, Bosch D, Gonzales-Dugo MP. Measuring surface roughness height to parameterize radar backscatter models for retrieval of surface soil moisture. *IEEE Geoscience and Remote Sensing Letters*. 2007; 4(1): 137-141.
14. Paglieroni DW, Chambers DH, Mast JE, Bond SW, Beer NR. Imaging modes for ground penetrating radar and their relation to detection performance. *IEEE Journal on Selected Topics in Applied Earth Observations and Remote Sensing*. 2015;8(3):1132–1144.
15. Soumekh M. Synthetic aperture radar signal processing. New York (NY): Wiley; 1999.

List of Symbols, Abbreviations, and Acronyms

2-D	two-dimensional
3-D	three-dimensional
ADC	analog-to-digital converter
CEH	counter explosive hazard
DRMS	distance root mean square
EM	electromagnetic
FDTD	finite-difference time-domain
GPR	ground-penetrating radar
GPS	global positioning system
H-H	horizontal-horizontal
LOS	line of sight
PSF	point spread function
PTR	point target response
RMS	root mean square
RTK	real-time kinematic
Rx	receiver
sUAV	small unmanned aerial vehicle
SAR	synthetic aperture radar
SNR	signal-to-noise ratio
Tx	transmitter
UWB	ultra-wideband
V-V	vertical-vertical

1 DEFENSE TECHNICAL
(PDF) INFORMATION CTR
DTIC OCA

2 CCDC ARL
(PDF) IMAL HRA
RECORDS MGMT
FCDD RLD CL
TECH LIB

1 GOVT PRINTG OFC
(PDF) A MALHOTRA

6 CCDC ARL
(PDF) FCDD RLS RU
A SULLIVAN
D LIAO
T DOGARU
C LE
B PHELAN
K SHERBONDY